
Improving Faithfulness for Vision Transformers

Lijie Hu ^{*,1,6}, Yixin Liu ^{*,2}, Ninghao Liu ³, Mengdi Huai ⁴, Lichao Sun ², and Di Wang ^{1,5,6}

¹ King Abdullah University of Science and Technology, ² Lehigh University

³ University of Georgia, ⁴ Iowa State University, ⁵ Computational Bioscience Research Center

⁶ SDAIA-KAUST Center of Excellence in Data Science and Artificial Intelligence
{lijie.hu, di.wang}@kaust.edu.sa, {yila22, lis221}@lehigh.edu, ninghao.liu@uga.edu, mdhuai@iastate.edu

Abstract

Vision Transformers (ViTs) have achieved state-of-the-art performance for various vision tasks. One reason behind the success lies in their ability to provide plausible innate explanations for the behavior of neural architectures. However, ViTs suffer from issues with explanation faithfulness, as their focal points are fragile to adversarial attacks and can be easily changed with even slight perturbations on the input image. In this paper, we propose a rigorous approach to mitigate these issues by introducing Faithful ViTs (FViTs). Briefly speaking, an FViT should have the following two properties: (1) The top- k indices of its self-attention vector should remain mostly unchanged under input perturbation, indicating stable explanations; (2) The prediction distribution should be robust to perturbations. To achieve this, we propose a new method called Denoised Diffusion Smoothing (DDS), which adopts randomized smoothing and diffusion-based denoising. We theoretically prove that processing ViTs directly with DDS can turn them into FViTs. We also show that Gaussian noise is nearly optimal for both ℓ_2 and ℓ_∞ -norm cases. Finally, we demonstrate the effectiveness of our approach through comprehensive experiments and evaluations. Specifically, we compare our FViTs with other baselines through visual interpretation and robustness accuracy under adversarial attacks. Results show that FViTs are more robust against adversarial attacks while maintaining the explainability of attention, indicating higher faithfulness.

1 Introduction

Transformers and attention-based frameworks have been widely adopted as benchmarks for natural language processing tasks Kenton and Toutanova (2019); Radford et al. (2019). Recently, their ideas also have been borrowed in many computer vision tasks such as image recognition Dosovitskiy et al. (2021), object detection Zhu et al. (2021), image processing Chen et al. (2021) and semantic segmentation Zheng et al. (2021). Among them, the most successful variant is the vision transformer (ViT) Dosovitskiy et al. (2021), which uses self-attention modules. Similar to tokens in the text domain, ViTs divide each image into a sequence of patches (visual tokens), and then feed them into self-attention layers to produce representations of correlations between visual tokens. The success of these attention-based modules is not only because of their good performance but also due to their “self-explanation” characteristics. Unlike post-hoc interpretation methods Du et al. (2019), attention weights can intrinsically provide the “inner-workings” of models Meng et al. (2019), i.e., the entries in attention vector could point us to the most relevant features of the input image for its prediction, and can also provide visualization for “where” and “what” the attention focuses on Xu et al. (2015).

As a crucial characteristic for explanation methods, faithfulness requires that the explanation method reflects its reasoning process Jacovi and Goldberg (2020). Therefore, for ViTs, their attention feature

*The first two authors contributed equally to this work.

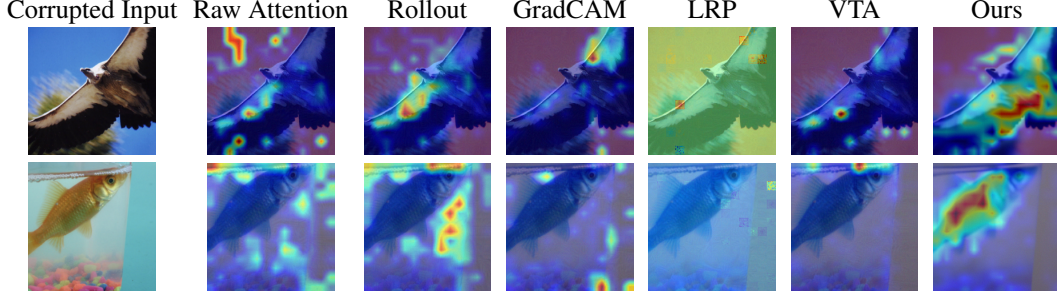


Figure 1: Visualization results of the attention map on corrupted input for different methods.

vectors should reveal what is essential to their prediction. Furthermore, faithfulness encompasses two properties: completeness and stability. Completeness means that the explanation should cover all relevant factors or patches related to its corresponding prediction Sundararajan et al. (2017), while stability ensures that the explanation is consistent with humans understanding and robust to slight perturbations. Based on these properties, we can conclude that “faithful ViTs” (FViTs) should have the **good robustness performance**, and certified **explainability** of attention maps which are **robust against perturbations**.

While the self-attention module in ViTs already possesses the property of completeness, it often suffers from stability issues. For example, in language tasks, Wiegrefe and Pinter (2019); Hu et al. (2022) have shown that attention is not robust, as a slight perturbation on the embedding vector can cause the attention vector distribution to change drastically. Similarly, for vision tasks, we find that such a phenomenon is not uncommon for ViTs, where attention modules are sensitive to perturbations on input images. For instance, in Fig. 1, we can see that a slight perturbation on the input image can cause the attention vector to focus on the wrong region for the image class, leading to an incorrect interpretation heat map and, consequently, confusing predictions. Actually, interpretation instability has also been identified as a pervasive issue in deep learning Ghorbani et al. (2019), where carefully-crafted small perturbations on the input can significantly change the interpretation result. Thus, stability has become an important factor for faithful interpretations. First, an unstable interpretation is prone to noise interference, hindering users’ understanding of the underlying reasoning behind model predictions. Second, instability undermines the reliability of interpretation as a diagnostic tool for models Ghorbani et al. (2019); Dombrowski et al. (2019); Yeh et al. (2019); Hu et al. (2022). Therefore, it is crucial to mitigate the issue of unstable explanations in ViTs.

Although ViTs have shown to be more robust in predictions than convolutional neural networks (CNNs) Bai et al. (2021); Paul and Chen (2022); Naseer et al. (2021), whether they can provide **faithful interpretations** remains uncertain. Compared to adversarial machine learning, which aims to enhance the robustness of classification accuracy, mitigating the unstable explanation issue in ViTs is more challenging. Here, we not only aim to improve the robustness of prediction performance but also, more importantly, **make the attention heat map robust to perturbations**. Therefore, a natural question arises: **can we develop provable and faithful variants of ViTs whose attention vectors and predictions are robust to perturbations?** In this paper, we provide an affirmative answer to this question. Specifically, our contributions can be summarized as follows.

1. We propose a formal and mathematical definition for FViTs. Specifically, an FViT must satisfy the following two properties for any input image: (1) It must ensure that the top- k indices of its attention feature vector remain relatively stable with perturbations, indicating interpretability stability. (2) However, attention vector stability alone cannot guarantee prediction robustness for FViTs. Therefore, an FViT must also ensure that its prediction distribution remains relatively stable under perturbations.
2. We propose a method called Denoised Diffusion Smoothing (DDS) to obtain FViTs. Surprisingly, we demonstrate that our DDS can directly transform ViTs into FViTs. Briefly speaking, DDS involves two main components: (1) the standard randomized smoothing with Gaussian noise and (2) a denoising diffusion probabilistic model. It is worth noting that prior work on randomized smoothing has focused on enhancing prediction robustness. In contrast, we demonstrate that randomized smoothing can also enhance the faithfulness of attention vectors in ViTs. Additionally, we demonstrate that Gaussian noise is near-optimal for our method in both the ℓ_2 -norm and ℓ_∞ -norm cases.

3. We conducted extensive experiments on three benchmark datasets using ViT, DeiT, and Swin models to verify the above two properties of the FViTs as claimed by our theories. Firstly, we demonstrate that our FViTs are more robust to different types of perturbations than other baselines. Secondly, we show the interpretability faithfulness of FViTs through visualization. Lastly, we verify our certified faithful region as claimed by our theories. The results reveal that our FViTs can provide provable faithful interpretations.

Due to space limitations, we have included details on theoretical proofs and additional experimental results in the Appendix section.

2 Related Work

Interpretability for computer vision tasks. Interpretation approaches in computer vision can be broadly categorized into two classes according to the part of models they participated in: post-hoc interpretation and self-explaining interpretation. Post-hoc interpretation methods require post-processing the model after training to explain the behaviors of black-box models. Typically, these methods either use surrogate models to explain local predictions Ribeiro et al. (2016), or adopt gradient perturbation methods Zeiler and Fergus (2014); Lundberg and Lee (2017) or feature importance methods Ross et al. (2017); Selvaraju et al. (2017). While post-hoc approaches require additional post-processing steps after the training process, self-explaining interpretation methods could be considered as integral parts of models, and they can generate explanations and make predictions simultaneously Li et al. (2018); Abnar and Zuidema (2020). From this view, ViTs can be considered as self-explaining interpretation approaches, as they use attention feature vectors to quantify the contributions of different tokens to their predictions.

Faithfulness in explainable methods. Faithfulness is a crucial property that explanation models should satisfy, ensuring that the explanation accurately reflects the true reasoning process of the model Wiegrefe and Pinter (2019); Herman (2017); Jacovi and Goldberg (2020); Lyu et al. (2022). Faithfulness is also related to other principles such as sensitivity, implementation invariance, input invariance, and completeness Yeh et al. (2019). Completeness refers to the explanation comprehensively covering all relevant factors to the prediction Sundararajan et al. (2017), while the other three terms are all related to the stability of different kinds of perturbations. The explanation should change if heavily perturbing the important features that influence the prediction Adebayo et al. (2018), but be stable to small perturbations Yin et al. (2022). Thus, stability is crucial to explanation faithfulness. Some preliminary work has been proposed to obtain stable interpretations. For example, Yeh et al. (2019) theoretically analyzes the stability of post-hoc interpretation and proposes the use of smoothing to improve interpretation stability. Yin et al. (2022) designs an iterative gradient descent algorithm to get a counterfactual interpretation, which shows desirable stability. However, these techniques are designed for post-hoc interpretation and cannot be directly applied to attention-based mechanisms like ViTs.

Robustness for ViTs. There is also a substantial body of work on achieving robustness for ViTs, including studies such as Mahmood et al. (2021); Salman et al. (2022); Aldahdooh et al. (2021); Naseer et al. (2021); Paul and Chen (2022); Mao et al. (2022). However, these studies exclusively focus on improving the model’s robustness in terms of its prediction, without considering the stability of its interpretation (i.e., attention feature vector distribution). While we do employ the randomized smoothing approach commonly used in adversarial machine learning, our primary objective is to maintain the top- k indices unchanged under perturbations. And we introduce DDS, which leverages a smoothing-diffusion process to obtain faithful ViTs while also enhancing prediction performance.

3 Vanilla Vision Transformers

In this paper, we adopt the notation introduced in Zhou et al. (2022) to describe ViTs. ViTs process an input image x by first dividing it into n uniform patches. Each patch is then represented as a token embedding, denoted as $x_i \in \mathbb{R}^q$ for $i = 1, \dots, n$. The token embeddings are then fed into a stack of transformer blocks, which use self-attention for token mixing and MLPs for channel-wise feature transformation.

Token mixing. A ViT makes use of the self-attention mechanism to aggregate global information. Given an input token embedding tensor $X = [x_1, \dots, x_n] \in \mathbb{R}^{q \times n}$, self-attention applies linear transformations with parameters W_K, W_Q , to embed X into a key $K = W_K X \in \mathbb{R}^{q \times n}$ and a query $Q = W_Q X \in \mathbb{R}^{q \times n}$ respectively. The self-attention module then calculates the attention matrix and aggregates the token features as follows:

$$Z^\top = \text{self-attention}(X) = \text{softmax}\left(\frac{Q^\top K}{\sqrt{q}}\right) V^\top W_L, \quad (1)$$

where $Z = [z_1, \dots, z_n]$ is the aggregated token feature, $W_L \in \mathbb{R}^{q \times q}$ is a linear transformation, and \sqrt{q} is a scaling factor. The output of the self-attention is normalized with Layer-norm and fed into an MLP to generate the input for the next block. At the final layer, the ViT outputs a prediction vector. It is worth highlighting that the self-attention mechanism can be viewed as a function that maps each image $X \in \mathbb{R}^{q \times n}$ to an attention feature vector $Z(X) \in \mathbb{R}^n$.

4 Towards Faithful Vision Transformers

As mentioned in the introduction, improving the stability and robustness of the self-attention modules in ViTs is crucial for making them more faithful. However, when it comes to explanation methods, it is not only important to consider the robustness of the model’s prediction under perturbations but also the sensitivity and stability of its explanation modules. Specifically, **the explanation modules should be sensitive enough to important token perturbations while remaining stable under noise perturbations**. As the attention mechanism in ViTs outputs a vector indicating the importance of each visual token, it is necessary to reconsider the robustness of both the attention module and ViTs. In general, a faithful ViT should satisfy the following two properties:

1. The magnitude of each entry in the attention vector indicates the importance of its associated patch. To ensure interpretability robustness, it is sufficient to maintain the order of leading entries. We measure interpretability robustness by computing the overlap of the top- k indices between the attention vector of the original input and the perturbed input, where k is a hyperparameter.
2. The attention vector is fed to an MLP for prediction. In addition to the robustness for top- k indices, a robust attention vector should also preserve the final model prediction. Specifically, we aim for the prediction distribution based on the robust attention under perturbations is almost the same as the distribution without perturbation. We measure the similarity or closeness between these distributions using different divergences.

4.1 Motivation and Challenges

Motivation. Although some literature has addressed methods to improve the robustness of ViTs, to the best of our knowledge, this is the first paper to propose a solution that enhances the faithfulness of ViTs while providing provable FViTs. Our work fills a gap in addressing both the robustness and interpretability of ViTs, as demonstrated through both theoretical analysis and empirical experiments.

Why stability of attention vectors’ top- k indices cannot imply the robustness of prediction?

While ensuring the stability of the top- k indices of the attention vectors is crucial for interpretability, it does not necessarily guarantee the robustness of the final prediction. This is because the stability of the prediction is also dependent on the magnitude of the entries associated with the top- k indices. For instance, consider the vectors $v_1 = (0.1, 0.2, 0.5, 0.7)$ and $v_2 = (0.2, 0.8, 0.9, 2)$, which have the same top indices. However, the difference in their magnitudes can significantly affect the final prediction. Therefore, in addition to ensuring the stability of the top- k indices, an FViT should also meet the requirement that its prediction distribution remains relatively unchanged under perturbations to achieve robustness.

Technical Challenges. The technical challenges of this paper are twofold. First, we need to give a definition of FViTs which contains the conditions that can quantify the stability of both the attention vectors and the model prediction under perturbations. This is challenging because we need to balance the sensitivity and stability of the explanation modules, and also consider the trade-off between interpretability and utility. Addressing these technical challenges is critical to achieving the main objective of this paper, which is to provide faithful ViTs. Second, we need to design an efficient and effective algorithm to generate noise to preserve the robustness and interpretability of ViTs. This is

challenging because standard noise methods may cause significant changes to the attention maps, which could lead to inaccurate and misleading explanations. To tackle this challenge, we introduce a mathematically-proven approach for noise generation and leverage denoised diffusion to balance the utility and interpretability trade-off, which is non-trivial and provable. Also, this study is the first to demonstrate its effectiveness in enhancing explanation faithfulness, providing rigorous proof, and certifying the faithfulness of ViTs.

4.2 Definition of FViTs

In the following, we will mathematically formulate our above intuitions. Before that, we first give the definition of the top- k overlap ratio for two vectors.

Definition 4.1. For vector $x \in \mathbb{R}^n$, we define the set of top- k component $T_k(\cdot)$ as

$$T_k(x) = \{i : i \in [d] \text{ and } |\{x_j \geq x_i : j \in [n]\}| \leq k\}.$$

And for two vectors x, x' , their top- k overlap ratio $V_k(x, x')$ is defined as $V_k(x, x') = \frac{1}{k} |T_k(x) \cap T_k(x')|$.

Definition 4.2 (Faithful ViTs). We call a function $f : \mathbb{R}^{q \times n} \mapsto \mathbb{R}^n$ is an $(R, D, \gamma, \beta, k, \|\cdot\|)$ -*faithful attention module* for ViTs if for any given input data x and for all $x' \in \mathbb{R}^{q \times n}$ such that $\|x - x'\| \leq R$, $f(x')$ satisfies

1. (Top- k Robustness) $V_k(f(x'), f(x)) \geq \beta$.
2. (Prediction Robustness) $D(\bar{y}(x), \bar{y}(x')) \leq \gamma$, where $\bar{y}(x), \bar{y}(x')$ are the prediction distribution of ViTs based on $f(x), f(x')$ respectively.

We also call the vector $f(x)$ as an $(R, D, \gamma, \beta, k, \|\cdot\|)$ -*faithful attention* for x , and the models of ViTs based on f as *faithful ViTs* (FViTs).

We can see there are several terms in the above definition. Specifically, R represents the faithful radius which measures the faithful region; D is a metric of the similarity between two distributions which could be a distance or a divergence; γ measures the closeness of the two prediction distributions; $0 < \beta < 1$ is the robustness of top- k indices; $\|\cdot\|$ is some norm. When γ is smaller or β is larger, then the attention module will be more robust, and thus will be more faithful. In this paper, we will focus on the case where divergence D is the Rényi divergence and $\|\cdot\|$ is either the ℓ_2 -norm or the ℓ_∞ -norm (if we consider x as a $d = q \times n$ dimensional vector), as we can show if the prediction distribution is robust under Rényi divergence, then the prediction will be unchanged with perturbations on input Li et al. (2019).

Definition 4.3. Given two probability distributions P and Q , and $\alpha \in (1, \infty)$, the α -Rényi divergence $D_\alpha(P||Q)$ is defined as $D_\alpha(P||Q) = \frac{1}{\alpha-1} \log \mathbb{E}_{x \sim Q}(\frac{P(x)}{Q(x)})^\alpha$.

Theorem 4.4. If a function is a $(R, D_\alpha, \gamma, \beta, k, \|\cdot\|)$ -*faithful attention module* for ViTs, then if

$$\gamma \leq -\log(1 - p_{(1)} - p_{(2)} + 2(\frac{1}{2}(p_{(1)}^{1-\alpha} + p_{(2)}^{1-\alpha}))^{\frac{1}{1-\alpha}}),$$

we have for all x' such that where $\|x - x'\| \leq R$, $\arg \max_{g \in \mathcal{G}} \mathbb{P}(\bar{y}(x) = g) = \arg \max_{g \in \mathcal{G}} \mathbb{P}(\bar{y}(x') = g)$, where \mathcal{G} is the set of classes, $p_{(1)}$ and $p_{(2)}$ refer to the largest and the second largest probabilities in $\{p_i\}$, where p_i is the probability that $\bar{y}(x)$ returns the i -th class.

5 Finding Faithful Vision Transformers

5.1 ℓ_2 -norm Case

In the previous section, we introduced faithful attention and FViTs, now we want to design algorithms to find such a faithful attention module. We notice that in faithful attention, the condition of prediction robustness is quite close to adversarial machine training which aims to design classifiers that are robust against perturbations on inputs. Thus, a natural idea is to borrow the approaches in adversarial machine training to see whether they can get faithful attention modules. Surprisingly, we find that using randomized smoothing to the vanilla ViT, which is a standard method for certified robustness Cohen et al. (2019), and then applying a denoised diffusion probabilistic model Ho et al. (2020)

to the perturbed input can adjust it to an FViT. And its corresponding attention module becomes a faithful attention module. Specifically, for a given input image x , we preprocess it by adding some randomized Gaussian noise, i.e., $\tilde{x} = x + z$ with $z \sim \mathcal{N}(0, \sigma^2 I_{q \times n})$. Then we will denoise \tilde{x} via some denoised diffusion model to get \hat{x} , and feed the perturbed-then-denoised \hat{x} to the self-attention module Z in (1) and process to later parts of the original ViT to get the prediction. Thus, in total, we can represent the attention module as $\tilde{w}(x) = Z(T(x + z))$, where T represents the denoised diffusion method. Here we mainly adopt the denoising diffusion probabilistic model in Nichol and Dhariwal (2021); Ho et al. (2020); Carlini et al. (2023), which leverages off-the-shelf diffusion models as image denoiser. Specifically, it has the following steps after we add Gaussian noise to x and get \tilde{x} .

In the first step, we establish a connection between the noise models utilized in randomized smoothing and diffusion models. Specifically, while randomized smoothing augments data points with additive Gaussian noise i.e., $x_{\text{rs}} \sim \mathcal{N}(x, \sigma^2 \mathbf{I})$, diffusion models rely on a noise model of the form $x_t \sim \mathcal{N}(\sqrt{\alpha_t}x, (1 - \alpha_t)\mathbf{I})$, where the factor α_t is a constant derived from the timestamp t . To employ a diffusion model for randomized smoothing, DDS scales x_{rs} by $\sqrt{\alpha_t}$ and adjusts the variances to obtain the relationship $\sigma^2 = \frac{1 - \alpha_t}{\alpha_t}$. The formula for this equation may vary depending on the schedule of the α_t terms employed by the diffusion model, but it can be calculated in closed form.

Using this calculated timestep, we can then compute $x_{t^*} = \sqrt{\alpha_{t^*}}(x + \delta)$, where $\delta \sim \mathcal{N}(0, \sigma^2 \mathbf{I})$, and apply a diffusion denoiser on x_{t^*} to obtain an estimate of the denoised sample, $\hat{x} = \text{denoise}(x_{t^*}; t^*)$. To further enhance the robustness, we repeat this denoising process multiple times (e.g., 100,000). The details of our method, namely Denoised Diffusion Smoothing (DDS), are shown in Algorithm 1 in Appendix.

In the following, we will show \tilde{w} is a faithful attention module. Before showing the results, we first provide some notations. For input image x , we denote \tilde{w}_{i^*} as the i -th largest component in $\tilde{w}(x)$. Let $k_0 = \lfloor (1 - \beta)k \rfloor + 1$ as the minimum number of changes on $\tilde{w}(x)$ to make it violate the β -top- k overlapping ratio with $\tilde{w}(x)$. Let \mathcal{S} denote the set of last k_0 components in top- k indices and the top k_0 components out of top- k indices.

Theorem 5.1. *Consider the function \tilde{w} where $\tilde{w}(x) = Z(T(x + z))$ with Z in (1), T as the denoised diffusion model and $z \sim \mathcal{N}(0, \sigma^2 I_{q \times n})$. Then it is an $(R, D_\alpha, \gamma, \beta, k, \|\cdot\|_2)$ -faithful attention module for ViTs for any $\alpha > 1$ if for any input image x we have*

$$\sigma^2 \geq \max\{\alpha R^2/2(\frac{\alpha}{\alpha-1} \ln(2k_0(\sum_{i \in \mathcal{S}} \tilde{w}_{i^*}^\alpha)^{\frac{1}{\alpha}} + (2k_0)^{\frac{1}{\alpha}} \sum_{i \notin \mathcal{S}} \tilde{w}_{i^*}) - \frac{1}{\alpha-1} \ln(2k_0)), \alpha R^2/2\gamma\}.$$

Theorem 5.1 indicates that $\tilde{w}(x)$ will be faithful attention for input x when σ^2 is large enough. Equivalently, based on Theorem 5.1 and 4.4 we can also find a faithful region given β and k . Note that in practice it is hard to determine the specific α in Rényi divergence. Thus, we can take the supreme w.r.t all $\alpha > 1$ in finding the faithful region. See Algorithm 2 in Appendix for details.

We have shown that adding some Gaussian noise to the original data could get faithful attention through the original attention module. A natural question is whether adding Gaussian noise can be further improved by using other kinds of noise. Below we show that **Gaussian noise is already near optimal** for certifying a faithful attention module via randomized smoothing.

Theorem 5.2. *Consider any function $\tilde{w} : \mathbb{R}^{q \times n} \mapsto \mathbb{R}^n$ where $\tilde{w}(x) = Z(T(x + z))$ with some random noise z , T as the denoised diffusion model and Z in (1). Then if it is an $(R, D_\alpha, \gamma, \beta, k, \|\cdot\|_2)$ -faithful attention module for ViTs with sufficiently large α and $\mathbb{E}[\|z\|_{\max}] \leq \tau$ holds for sufficiently small $\tau = O(1)$. Then it must be true that $\tau \geq \Omega(\frac{\sqrt{\alpha}R}{\sqrt{\gamma}})$. Here for an matrix $z \in \mathbb{R}^{q \times n}$, $\|z\|_{\max}$ is defined as $\max_{i \in [q], j \in [n]} \|z_{i,j}\|$ is the maximal magnitude among all the entries in z .*

Note that in Theorem 5.1 we can see when γ is small enough then \tilde{w} will be a $(R, D_\alpha, \gamma, \beta, k, \|\cdot\|_2)$ -faithful attention module if $z \sim \mathcal{N}(0, \sigma^2 I_{q \times n})$ with $\sigma = \frac{\alpha R^2}{2\gamma}$. In this case we can see $\mathbb{E}\|z\|_{\max} = O(\frac{\log(q \cdot n)\sqrt{\alpha}R}{\sqrt{\gamma}})$. Thus, the Gaussian noise is optimal up to some logarithmic factors.

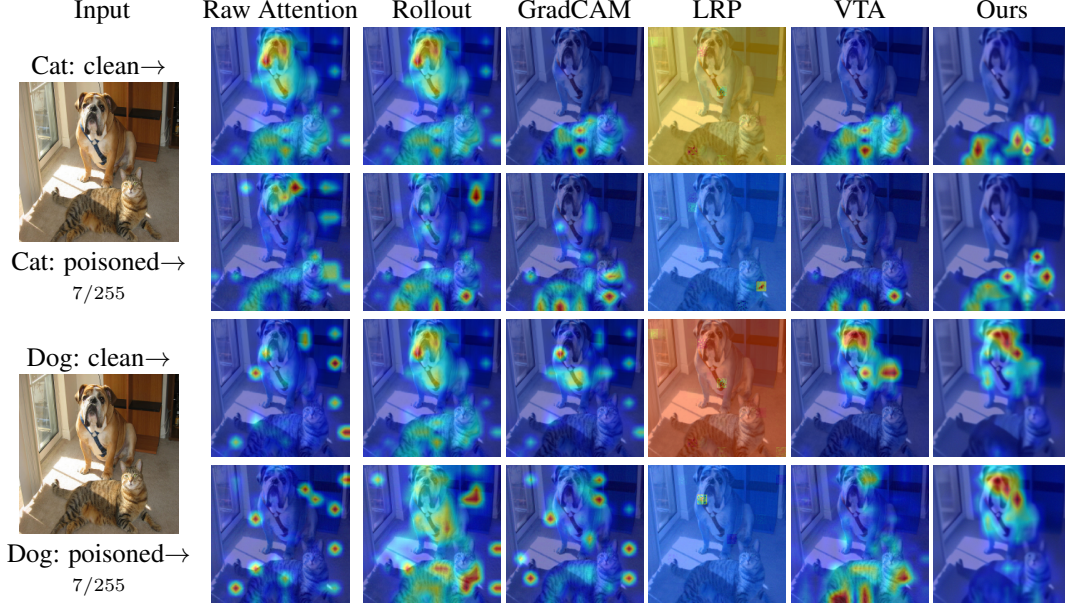


Figure 2: Class-specific explanation heat map visualizations under adversarial corruption. For each image, we present results for two different classes. Other baselines either give inconsistent interpretations or show wrong focus class regions under adversarial perturbations. While our method gives a consistent interpretation map and is robust against adversarial attacks.

5.2 ℓ_∞ -norm Case

In this section we consider the ℓ_∞ -norm instead of the ℓ_2 -norm. Surprisingly, we show that using the same method as above, we can still get a faithful attention module. Moreover, the Gaussian noise is still near-optimal.

Theorem 5.3. *Consider the function \tilde{w} where $\tilde{w}(x) = Z(T(x + z))$ with Z in (1), T as the denoised diffusion model and $z \sim \mathcal{N}(0, \sigma^2 I_{q \times n})$. Then it is an $(R, D_\alpha, \gamma, \beta, k, \|\cdot\|_\infty)$ -faithful attention module for ViTs for $\alpha > 1$ if for any input image x we have the following, where $d = q \cdot n$.*

$$\sigma^2 \geq \max\left\{d\alpha R^2/2\left(\frac{\alpha}{\alpha-1} \ln(2k_0\left(\sum_{i \in \mathcal{S}} \tilde{w}_{i*}^\alpha\right)^{\frac{1}{\alpha}} + (2k_0)^{\frac{1}{\alpha}} \sum_{i \notin \mathcal{S}} \tilde{w}_{i*}\right) - \frac{1}{\alpha-1} \ln(2k_0)\right), d\alpha R^2/2\gamma\right\}.$$

Compared with the result in Theorem 5.1 for the ℓ_2 -norm case, we can see there is the additional factor of d in the bound of the noise. This means if we aim to achieve the same faithful level as in the ℓ_2 -norm case, then in the ℓ_∞ -norm case we need to enlarge the noise by a factor of d . Equivalently, if we add the same scale of noise, then the faithful region for ℓ_∞ -norm will be shrunk by a factor of d of the region for ℓ_2 -norm. See Algorithm 2 for details.

Theorem 5.4. *Consider any function $\tilde{w} : \mathbb{R}^{q \times n} \mapsto \mathbb{R}^n$ where $\tilde{w}(x) = Z(T(x + z))$ with some random noise z and Z in (1). Then if it is an $(R, D_\alpha, \gamma, \beta, k, \|\cdot\|_\infty)$ -faithful attention module for ViTs with sufficiently large α and $\mathbb{E}[\|z\|_{\max}] \leq \tau$ holds for sufficiently small $\tau \leq O(1)$. Then it must be true that $\tau \geq \Omega(\frac{\sqrt{\alpha}R}{\sqrt{d}\gamma})$.*

Theorem 5.1 we can see when γ is small enough then \tilde{w} will an $(R, D_\alpha, \gamma, \beta, k, \|\cdot\|_\infty)$ -faithful attention module if $z \sim \mathcal{N}(0, \sigma^2 I_{q \times n})$ with $\sigma = \frac{d\alpha R^2}{2\gamma}$. In this case we can see $\mathbb{E}[\|z\|_{\max}] = O(\frac{\log(q \cdot n)\sqrt{d\alpha}R}{\sqrt{\gamma}})$. Thus, the Gaussian noise is optimal up to some logarithmic factors.

6 Experiments

In this section, we present experimental results on evaluating the interpretability and utility of our FViTs on various datasets and tasks. **More detailed implementation setup and additional experiments are in Appendix.**

Model	Method	ImageNet				Cityscape		COCO	
		Cla. Acc.	Pix. Acc.	mIoU	mAP	Pix. Acc.	mIoU	Pix. Acc.	mIoU
ViT	Raw Attention	0.78	0.65	0.54	0.82	0.72	0.62	0.8	0.7
	Rollout	0.79	0.67	0.56	0.84	0.74	0.64	0.82	0.72
	GradCAM	0.8	0.69	0.58	0.86	0.76	0.66	0.84	0.74
	LRP	0.81	0.71	0.6	0.88	0.78	0.68	0.86	0.76
	VTA	0.82	0.73	0.62	0.9	0.8	0.7	0.88	0.78
	Ours	0.85	0.76	0.65	0.93	0.83	0.73	0.91	0.81
DeiT	Raw Attention	0.79	0.66	0.55	0.83	0.73	0.63	0.81	0.71
	Rollout	0.8	0.68	0.57	0.85	0.75	0.65	0.83	0.73
	GradCAM	0.81	0.7	0.59	0.87	0.77	0.67	0.85	0.75
	LRP	0.82	0.72	0.61	0.89	0.79	0.69	0.87	0.77
	VTA	0.83	0.74	0.63	0.91	0.81	0.71	0.89	0.79
	Ours	0.86	0.77	0.66	0.94	0.84	0.74	0.89	0.79
Swin	Raw Attention	0.8	0.67	0.56	0.84	0.74	0.64	0.82	0.72
	Rollout	0.81	0.69	0.58	0.86	0.76	0.66	0.84	0.74
	GradCAM	0.82	0.71	0.6	0.88	0.78	0.68	0.86	0.76
	LRP	0.83	0.73	0.62	0.9	0.8	0.7	0.88	0.78
	VTA	0.84	0.75	0.64	0.92	0.82	0.72	0.9	0.8
	Ours	0.87	0.78	0.67	0.95	0.85	0.75	0.93	0.83

Table 1: Performance comparison of different methods on ImageNet, Cityscape, and COCO using three different ViT-based models under the default attack.

6.1 Experimental Setup

Datasets, tasks and network architectures. We consider two different tasks: classification and segmentation. For the classification task, we use ILSVRC-2012 ImageNet. And for segmentation, we use ImageNet-segmentation subset Guillaumin et al. (2014), COCO Lin et al. (2014), and Cityscape Cordts et al. (2016). To demonstrate our method is architectures-agnostic, we use three different ViT-based models, including Vanilla ViT Dosovitskiy et al. (2021), DeiT Touvron et al. (2021), and Swin ViT Liu et al. (2021).

Threat model. We focus on l_2 -norm bounded and l_∞ -norm bounded noises under a white-box threat model assumption for adversarial perturbations. The radius of adversarial noise ρ_u was set as $8/255$ by default. We employ the PGD Madry et al. (2017) algorithm to craft adversarial examples with a step size of $2/255$ and a total of 10 steps.

Baselines and attention map backbone. Since our DDS method can be used as a plugin to provide certified faithfulness for interpretability under adversarial attacks, regardless of the method used to generate attention maps. We set the standard deviation $\delta = 8/255$ for the Gaussian noise in our method as default. In this paper, we leverage Trans. Att. Chefer et al. (2021) as our explanation tool, which is a state-of-the-art method for generating class-aware interpretable attention maps. Several methods aim to improve the interpretability of attention maps, we include five baselines for comparison, including Raw Attention Vaswani et al. (2017), Rollout Abnar and Zuidema (2020), GradCAM Selvaraju et al. (2017), LRP Binder et al. (2016), and Vanilla Trans. Att. (VTA) Chefer et al. (2021).

Evaluation metrics. To demonstrate the utility of our approach, we report the classification accuracy on test data for classification tasks. As for the interpretability of our approach, we seek to evaluate the explanation map by leveraging the label of segmentation task as ‘ground truth’ following Chefer et al. (2021). To be specific, we compare the explanation map with the ground truth segmentation map. We measure the interpretability using pixel accuracy, mean intersection over union (mIoU) Varghese et al. (2020), and mean average precision (mAP) Henderson and Ferrari (2017). Note that pixel accuracy is calculated by thresholding the visualization by the mean value, while mAP uses the soft-segmentation to generate a score that is not affected by the threshold. Following conventional practices, we also report the results for negative and positive perturbation (pixels-erasing) tests Chefer et al. (2021). The area-under-the-curve (AUC) measured by erasing between 10% – 90% of the pixels is used to indicate the performance of explanation methods for both perturbations. For negative perturbation, a higher AUC indicates a more faithful interpretation since a good explanation should maintain accuracy after removing unrelated pixels (also referred to as input invariance Kindermans et al. (2019)). On the other hand, for positive perturbations, we expect to see a steep decrease in

performance after removing the pixels that are identified as important, where a lower AUC indicates the interpretation is better. We term the AUC of such perturbation tests as P-AUC. Furthermore, to ensure fair comparisons, we plot the P-AUC-radius curve under adversarial perturbations with a wide range of radii.

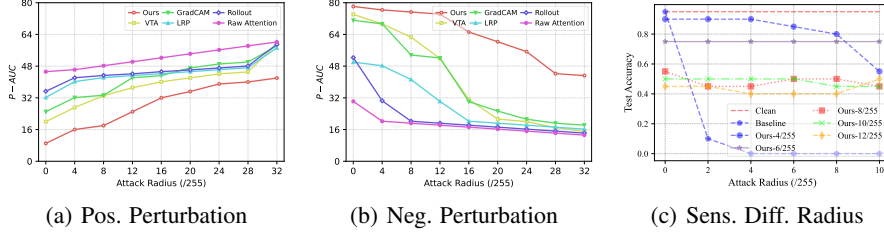


Figure 3: (a) and (b) are results of the perturbation test. (c) is the sensitivity analysis results.

6.2 Evaluating Interpretability and Utility

Classification and segmentation results. Based on the results shown in Table 1, it is obvious that our method is more robust and effective for all three datasets. Moreover, across all metrics, our method consistently outperforms other methods for all model architectures. For example, on ImageNet, our method achieves the highest classification accuracy (0.85) and pixel accuracy (0.76) for the ViT model and the highest mean IoU (0.66) and mean AP (0.94) for the DeiT model. These results suggest that our method could even outperform the previous methods on accuracy, and it is more faithful in identifying the most relevant features for image classification under malicious adversarial attacks compared to other methods. Please refer to Table 4 and 7 in the Appendix for complete results across different levels of perturbation.

Additionally, Figure 4, 6, and 7 in Appendix demonstrate visual comparisons of our method with baselines under adversarial attacks. It is clear that the baseline methods produce inconsistent results, while our method produces more consistent and clear visualizations even under data corruption. Moreover, as shown in Figure 2 (more results are in Appendix Figure 5 and 9), when analyzing images with two objects from different classes under adversarial perturbations, all previous methods produce similar but worse visualizations for each class. Surprisingly, our method is able to provide accurate and distinct visualization maps for each class despite adversarial perturbations. This indicates that our method is more faithful which is robust class-aware under attacks.

Perturbation tests. The results on Pos. perturbation in Figure 3(a) show that the P-AUC of our method consistently achieves the lowest value when we perform attacks with a radius ranging from 0/255 to 32/255, which suggests that our method are more faithful and interpretable. Similarly, as for Neg. perturbation, the results in Figure 3(b) also suggest that our method is more robust than other baselines when removing unrelated pixels, and indicate that our method can identify important pixels under corruptions.

Ablation study. The results are shown in Table 2 of the Appendix highlighting the crucial role that the denoising diffusion model and randomized smoothing play in the effectiveness of DDS. As we can see from the table, removing either of the components leads to a significant decrease in performance (under adversarial attacks) across all three evaluation metrics: classification accuracy, segmentation accuracy, and P-AUC. In particular, the classification and segmentation accuracy will decrease by 3.1% when the denoising step is removed, and by 1.3% and 1.5%, respectively when the randomized smoothing is eliminated. Moreover, we visualized the ablated version of our method in Figure 8. It is noteworthy that the performance degradation becomes more pronounced when both components are removed, compared to when only a single component is removed. This suggests that these two components are highly effective in improving the faithfulness of model prediction and explanation.

Sensitivity analysis. To evaluate the sensitivity of standard deviation δ of the added Gaussian noise, we conduct adversarial attacks on the ImageNet dataset with different δ for a certain number of data samples. We conduct testing under $\delta \in \{4/255, 6/255, 8/255, 10/255, 12/255\}$ and attack radius $\rho_a \in \{0, 2/255, 4/255, 6/255, 8/255, 10/255\}$. The results in Figure 3(c) suggest that, for the cases of $\delta = 4/255$ and $\delta = 6/255$, compared to the vanilla baseline, i.e., without any processing of

images, our method is able to prevent the testing accuracy from dropping significantly as the attack radius increase. However, we find that larger δ does not significantly decrease test accuracy when δ exceeds some threshold ($\delta = 8/255 - 12/255$). These results suggest that our method is sensitive to the selection of δ when δ is small, and it becomes insensitive when δ is larger. Nevertheless, across different δ , our method outperforms the baseline in terms of utility.

	Classification	Segementation		Perturbation Tests	
	Rob. Acc. (%)	Rob. Acc. (%)	mIOU	Pos. P -AUC	Neg. P -AUC
Ours	99.5	97.8	0.985	15.29	63.23
–smoothing	98.2	96.3	0.977	18.51	54.65
–denosing	96.4	94.7	0.965	21.36	50.53
–both	92.1	90.5	0.947	38.13	48.58

Table 2: Results of the ablation study on classification, segmentation, and perturbation tests.

Verifying faithful region. To verify the proposed faithful region estimation in Algorithm 2, we conduct an adversarial attack using projected gradient descent on our denoised smoothing classifier following Cohen et al. (2019). Given the faithful region radius $R(\delta) = \min\{P(\delta), Q(\delta)\}$ obtained in Algorithm 2, we attempt to find an adversarial example for our denoised smoothing classifier within radii of $1.5R$ or $2R$, under the condition that the example has been correctly classified within faithful region R . We succeed in finding such adversarial examples 23% of the time at a radius $1.5R$ and 64% of the time in a radius $2R$ on the ImageNet. These results empirically demonstrate the tightness of our proposed faithful bound.

6.3 Computational Cost

Our denoising algorithm is actually quite fast, for example, under the noise level of $\frac{8}{255}$, in each denoising trail, it only requires one forward step in adding a random Gaussian noise and $t^* = 45$ backward steps for denoising, which empirically takes about 0.32 seconds per images (256x256) on ImageNet 3. This shows that our methods are efficient and promising for real-world applications with large-scale data.

$ \delta _\infty$	2/255	4/255	8/255	12/255	16/255
t^*	0	8	45	107	193
Total Time(s)	0.60	3.18	3.20	3.25	3.33
Per Sample(s)	0.060	0.318	0.320	0.325	0.333

Table 3: The time cost of denoising under different noise levels with a total sample size of 10.

7 Conclusion

We proposed Faithful Vision Transformers (FViTs) to certify faithfulness in vanilla ViTs. We first gave a rigorous definition for FViTs. Then we proposed a method namely DDS, and theoretically proved that DDS can achieve robustness for both explainability and prediction. And this study is the first to demonstrate its effectiveness in enhancing explanation faithfulness, providing rigorous proofs, and certifying the faithfulness of ViTs. Finally, we showed faithfulness in FViTs via comprehensive experiments.

References

- Kenton, J. D. M.-W. C.; Toutanova, L. K. BERT: Pre-training of Deep Bidirectional Transformers for Language Understanding. Proceedings of NAACL-HLT. 2019; pp 4171–4186.
- Radford, A.; Wu, J.; Child, R.; Luan, D.; Amodei, D.; Sutskever, I.; others Language models are unsupervised multitask learners. *OpenAI blog* **2019**, 1, 9.
- Dosovitskiy, A.; Beyer, L.; Kolesnikov, A.; Weissenborn, D.; Zhai, X.; Unterthiner, T.; Dehghani, M.; Minderer, M.; Heigold, G.; Gelly, S.; Uszkoreit, J.; Houlsby, N. An Image is Worth 16x16 Words: Transformers for Image Recognition at Scale. International Conference on Learning Representations. 2021.

- Zhu, X.; Su, W.; Lu, L.; Li, B.; Wang, X.; Dai J F, D. D. Deformable transformers for end-to-end object detection. Proceedings of the 9th International Conference on Learning Representations. Virtual Event, Austria: OpenReview. net. 2021.
- Chen, H.; Wang, Y.; Guo, T.; Xu, C.; Deng, Y.; Liu, Z.; Ma, S.; Xu, C.; Xu, C.; Gao, W. Pre-trained image processing transformer. Proceedings of the IEEE/CVF Conference on Computer Vision and Pattern Recognition. 2021; pp 12299–12310.
- Zheng, S.; Lu, J.; Zhao, H.; Zhu, X.; Luo, Z.; Wang, Y.; Fu, Y.; Feng, J.; Xiang, T.; Torr, P. H.; others Rethinking semantic segmentation from a sequence-to-sequence perspective with transformers. Proceedings of the IEEE/CVF conference on computer vision and pattern recognition. 2021; pp 6881–6890.
- Du, M.; Liu, N.; Hu, X. Techniques for interpretable machine learning. *Communications of the ACM* **2019**, *63*, 68–77.
- Meng, L.; Zhao, B.; Chang, B.; Huang, G.; Sun, W.; Tung, F.; Sigal, L. Interpretable spatio-temporal attention for video action recognition. Proceedings of the IEEE/CVF International Conference on Computer Vision Workshops. 2019; pp 0–0.
- Xu, K.; Ba, J.; Kiros, R.; Cho, K.; Courville, A.; Salakhudinov, R.; Zemel, R.; Bengio, Y. Show, attend and tell: Neural image caption generation with visual attention. International conference on machine learning. 2015; pp 2048–2057.
- Jacovi, A.; Goldberg, Y. Towards Faithfully Interpretable NLP Systems: How Should We Define and Evaluate Faithfulness? Proceedings of the 58th Annual Meeting of the Association for Computational Linguistics. 2020; pp 4198–4205.
- Sundararajan, M.; Taly, A.; Yan, Q. Axiomatic attribution for deep networks. International conference on machine learning. 2017; pp 3319–3328.
- Wiegrefe, S.; Pinter, Y. Attention is not not Explanation. Proceedings of the 2019 Conference on Empirical Methods in Natural Language Processing and the 9th International Joint Conference on Natural Language Processing (EMNLP-IJCNLP). 2019; pp 11–20.
- Hu, L.; Liu, Y.; Liu, N.; Huai, M.; Sun, L.; Wang, D. SEAT: Stable and Explainable Attention. *arXiv preprint arXiv:2211.13290* **2022**,
- Ghorbani, A.; Abid, A.; Zou, J. Interpretation of neural networks is fragile. Proceedings of the AAAI conference on artificial intelligence. 2019; pp 3681–3688.
- Dombrowski, A.-K.; Alber, M.; Anders, C.; Ackermann, M.; Müller, K.-R.; Kessel, P. Explanations can be manipulated and geometry is to blame. *Advances in Neural Information Processing Systems* **2019**, *32*.
- Yeh, C.-K.; Hsieh, C.-Y.; Suggala, A.; Inouye, D. I.; Ravikumar, P. K. On the (in) fidelity and sensitivity of explanations. *Advances in Neural Information Processing Systems* **2019**, *32*.
- Bai, Y.; Mei, J.; Yuille, A. L.; Xie, C. Are Transformers more robust than CNNs? *Advances in Neural Information Processing Systems* **2021**, *34*, 26831–26843.
- Paul, S.; Chen, P.-Y. Vision transformers are robust learners. Proceedings of the AAAI Conference on Artificial Intelligence. 2022; pp 2071–2081.
- Naseer, M. M.; Ranasinghe, K.; Khan, S. H.; Hayat, M.; Shahbaz Khan, F.; Yang, M.-H. Intriguing properties of vision transformers. *Advances in Neural Information Processing Systems* **2021**, *34*, 23296–23308.
- Ribeiro, M. T.; Singh, S.; Guestrin, C. " Why should i trust you?" Explaining the predictions of any classifier. Proceedings of the 22nd ACM SIGKDD international conference on knowledge discovery and data mining. 2016; pp 1135–1144.
- Zeiler, M. D.; Fergus, R. Visualizing and understanding convolutional networks. European conference on computer vision. 2014; pp 818–833.

- Lundberg, S. M.; Lee, S.-I. A unified approach to interpreting model predictions. *Advances in neural information processing systems* **2017**, *30*.
- Ross, A. S.; Hughes, M. C.; Doshi-Velez, F. Right for the Right Reasons: Training Differentiable Models by Constraining their Explanations. Proceedings of the Twenty-Sixth International Joint Conference on Artificial Intelligence, IJCAI-17. 2017; pp 2662–2670.
- Selvaraju, R. R.; Cogswell, M.; Das, A.; Vedantam, R.; Parikh, D.; Batra, D. Grad-cam: Visual explanations from deep networks via gradient-based localization. Proceedings of the IEEE international conference on computer vision. 2017; pp 618–626.
- Li, K.; Wu, Z.; Peng, K.-C.; Ernst, J.; Fu, Y. Tell me where to look: Guided attention inference network. Proceedings of the IEEE Conference on Computer Vision and Pattern Recognition. 2018; pp 9215–9223.
- Abnar, S.; Zuidema, W. Quantifying attention flow in transformers. *arXiv preprint arXiv:2005.00928* **2020**,
- Herman, B. The promise and peril of human evaluation for model interpretability. *arXiv preprint arXiv:1711.07414* **2017**,
- Lyu, Q.; Apidianaki, M.; Callison-Burch, C. Towards Faithful Model Explanation in NLP: A Survey. *arXiv preprint arXiv:2209.11326* **2022**,
- Adebayo, J.; Gilmer, J.; Muelly, M.; Goodfellow, I.; Hardt, M.; Kim, B. Sanity checks for saliency maps. *Advances in neural information processing systems* **2018**, *31*.
- Yin, F.; Shi, Z.; Hsieh, C.-J.; Chang, K.-W. On the Sensitivity and Stability of Model Interpretations in NLP. Proceedings of the 60th Annual Meeting of the Association for Computational Linguistics (Volume 1: Long Papers). 2022; pp 2631–2647.
- Mahmood, K.; Mahmood, R.; Van Dijk, M. On the robustness of vision transformers to adversarial examples. Proceedings of the IEEE/CVF International Conference on Computer Vision. 2021; pp 7838–7847.
- Salman, H.; Jain, S.; Wong, E.; Madry, A. Certified patch robustness via smoothed vision transformers. Proceedings of the IEEE/CVF Conference on Computer Vision and Pattern Recognition. 2022; pp 15137–15147.
- Aldahdooh, A.; Hamidouche, W.; Deforges, O. Reveal of vision transformers robustness against adversarial attacks. *arXiv preprint arXiv:2106.03734* **2021**,
- Mao, X.; Qi, G.; Chen, Y.; Li, X.; Duan, R.; Ye, S.; He, Y.; Xue, H. Towards robust vision transformer. Proceedings of the IEEE/CVF Conference on Computer Vision and Pattern Recognition. 2022; pp 12042–12051.
- Zhou, D.; Yu, Z.; Xie, E.; Xiao, C.; Anandkumar, A.; Feng, J.; Alvarez, J. M. Understanding the robustness in vision transformers. International Conference on Machine Learning. 2022; pp 27378–27394.
- Li, B.; Chen, C.; Wang, W.; Carin, L. Certified Adversarial Robustness with Additive Noise. *Advances in Neural Information Processing Systems*. 2019; pp 9459–9469.
- Cohen, J.; Rosenfeld, E.; Kolter, Z. Certified adversarial robustness via randomized smoothing. International Conference on Machine Learning. 2019; pp 1310–1320.
- Ho, J.; Jain, A.; Abbeel, P. Denoising diffusion probabilistic models. *Advances in Neural Information Processing Systems* **2020**, *33*, 6840–6851.
- Nichol, A. Q.; Dhariwal, P. Improved denoising diffusion probabilistic models. International Conference on Machine Learning. 2021; pp 8162–8171.
- Carlini, N.; Tramèr, F.; Dvijotham, K. D.; Rice, L.; Sun, M.; Kolter, J. Z. (Certified!!) Adversarial Robustness for Free! The Eleventh International Conference on Learning Representations. 2023.

- Guillaumin, M.; Küttel, D.; Ferrari, V. Imagenet auto-annotation with segmentation propagation. *International Journal of Computer Vision* **2014**, *110*, 328–348.
- Lin, T.-Y.; Maire, M.; Belongie, S.; Hays, J.; Perona, P.; Ramanan, D.; Dollár, P.; Zitnick, C. L. Microsoft coco: Common objects in context. European conference on computer vision. 2014; pp 740–755.
- Cordts, M.; Omran, M.; Ramos, S.; Rehfeld, T.; Enzweiler, M.; Benenson, R.; Franke, U.; Roth, S.; Schiele, B. The cityscapes dataset for semantic urban scene understanding. Proceedings of the IEEE conference on computer vision and pattern recognition. 2016; pp 3213–3223.
- Touvron, H.; Cord, M.; Douze, M.; Massa, F.; Sablayrolles, A.; Jégou, H. Training data-efficient image transformers & distillation through attention. International Conference on Machine Learning. 2021; pp 10347–10357.
- Liu, Z.; Lin, Y.; Cao, Y.; Hu, H.; Wei, Y.; Zhang, Z.; Lin, S.; Guo, B. Swin transformer: Hierarchical vision transformer using shifted windows. Proceedings of the IEEE/CVF International Conference on Computer Vision. 2021; pp 10012–10022.
- Madry, A.; Makelov, A.; Schmidt, L.; Tsipras, D.; Vladu, A. Towards deep learning models resistant to adversarial attacks. *arXiv preprint arXiv:1706.06083* **2017**,
- Chefer, H.; Gur, S.; Wolf, L. Transformer interpretability beyond attention visualization. Proceedings of the IEEE/CVF Conference on Computer Vision and Pattern Recognition. 2021; pp 782–791.
- Vaswani, A.; Shazeer, N.; Parmar, N.; Uszkoreit, J.; Jones, L.; Gomez, A. N.; Kaiser, Ł.; Polosukhin, I. Attention is all you need. *Advances in neural information processing systems* **2017**, *30*.
- Binder, A.; Montavon, G.; Lapuschkin, S.; Müller, K.-R.; Samek, W. Layer-wise relevance propagation for neural networks with local renormalization layers. International Conference on Artificial Neural Networks. 2016; pp 63–71.
- Varghese, S.; Bayzidi, Y.; Bar, A.; Kapoor, N.; Lahiri, S.; Schneider, J. D.; Schmidt, N. M.; Schlicht, P.; Huger, F.; Fingscheidt, T. Unsupervised temporal consistency metric for video segmentation in highly-automated driving. Proceedings of the IEEE/CVF Conference on Computer Vision and Pattern Recognition Workshops. 2020; pp 336–337.
- Henderson, P.; Ferrari, V. End-to-end training of object class detectors for mean average precision. Asian conference on computer vision. 2017; pp 198–213.
- Kindermans, P.-J.; Hooker, S.; Adebayo, J.; Alber, M.; Schütt, K. T.; Dähne, S.; Erhan, D.; Kim, B. *Explainable AI: Interpreting, Explaining and Visualizing Deep Learning*; Springer, 2019; pp 267–280.
- Liu, A.; Chen, X.; Liu, S.; Xia, L.; Gan, C. Certifiably Robust Interpretation via Renyi Differential Privacy. *arXiv preprint arXiv:2107.01561* **2021**,
- Dwork, C.; McSherry, F.; Nissim, K.; Smith, A. Calibrating noise to sensitivity in private data analysis. Theory of cryptography conference. 2006; pp 265–284.
- Mironov, I. Rényi differential privacy. 2017 IEEE 30th computer security foundations symposium (CSF). 2017; pp 263–275.
- Steinke, T.; Ullman, J. Between Pure and Approximate Differential Privacy. *Journal of Privacy and Confidentiality* **2016**, *7*.
- Chen, J.; Song, L.; Wainwright, M. J.; Jordan, M. I. L-shapley and c-shapley: Efficient model interpretation for structured data. *arXiv preprint arXiv:1808.02610* **2018**,
- Lee-Thorp, J.; Ainslie, J.; Eckstein, I.; Ontanon, S. Fnet: Mixing tokens with fourier transforms. *arXiv preprint arXiv:2105.03824* **2021**,
- Bach, S.; Binder, A.; Montavon, G.; Klauschen, F.; Müller, K.-R.; Samek, W. On pixel-wise explanations for non-linear classifier decisions by layer-wise relevance propagation. *PloS one* **2015**, *10*, e0130140.

Montavon, G.; Lapuschkin, S.; Binder, A.; Samek, W.; Müller, K.-R. Explaining nonlinear classification decisions with deep taylor decomposition. *Pattern recognition* **2017**, *65*, 211–222.

Jacobgil Jacobgil/VIT-explain: Explainability for Vision Transformers. <https://github.com/jacobgil/vit-explain>.

A Algorithms

Algorithm 1 FViTs via Denoised Diffusion Smoothing

- 1: **Input:** x ; A standard deviation $\sigma > 0$.
 - 2: t^* , find t s.t. $\frac{1-\alpha_t}{\alpha_t} = \sigma^2$.
 - 3: $x_{t^*} = \sqrt{\alpha_{t^*}}(\tilde{x} + \mathcal{N}(0, \sigma^2 \mathbf{I}))$.
 - 4: $\hat{x} = \text{denoise}(x_{t^*}; t^*)$.
 - 5: $w = \text{self-attention}(\hat{x})$.
 - 6: **Return:** attention weight w .
-

Algorithm 2 Finding the Faithfulness Region in FViTs

- 1: **Input:** Original self-attention module Z ; the standard deviation $\sigma > 0$; classifier of the original ViT \bar{y} ; Number of repetitions m . Input image x .
- 2: **for** $i \in [m]$ **do**
- 3: Sample a Gaussian noise $z_i \sim \mathcal{N}(0, \sigma^2 I_{q \times n})$ and add it to the input image x . Then get an attention vector $\tilde{w}_i = Z(T(x + z_i))$ via Algorithm 1 and feed it to the original ViT and get the prediction $c_i = \arg \max_{g \in \mathcal{G}} \bar{y}(x + z_i)$.
- 4: **end for**
- 5: Estimate the distribution of the output as $p_j = \frac{\#\{c_i=j; i=1, \dots, m\}}{m}$. Compute the average of \tilde{w}_i : $\tilde{w} = \frac{1}{m} \sum_{i=1}^m \tilde{w}_i$.
- 6: **For the ℓ_2 -norm case:** Calculate the upper bound P as the following:

$$\sup_{\alpha > 1} \left[-\frac{2\sigma^2}{\alpha} \ln(1 - p_{(1)} - p_{(2)}) + 2 \left(\frac{1}{2} (p_{(1)}^{1-\alpha} + p_{(2)}^{1-\alpha}) \right)^{\frac{1}{1-\alpha}} \right]^{1/2}$$

where $p_{(1)}$ and $p_{(2)}$ are the first and the second largest values in $\{p_i\}$. Then calculate the upper bound Q as

$$\sup_{\alpha > 1} \left[\frac{2\sigma^2}{\alpha} \left(\frac{\alpha}{\alpha - 1} \ln(2k_0 \left(\sum_{i \in \mathcal{S}} \tilde{w}_{i^*}^\alpha \right)^{\frac{1}{\alpha}} + (2k_0)^{\frac{1}{\alpha}} \sum_{i \notin \mathcal{S}} \tilde{w}_{i^*}) - \frac{1}{\alpha - 1} \ln(2k_0) \right) \right]^{1/2},$$

where \tilde{w}_{i^*} is the i -th largest component in \tilde{w} , $k_0 = \lfloor (1 - \beta)k \rfloor + 1$, and \mathcal{S} denotes the set of last k_0 components in top- k indices and the top k_0 components out of top- k indices.

- 7: **For the ℓ_∞ -norm case:** Calculate $P = \frac{\tilde{P}}{d}$ and $Q = \frac{\tilde{Q}}{d}$, where \tilde{P} and \tilde{Q} is equivalent to P and Q in the ℓ_2 -norm case respectively, $d = q \times n$.
 - 8: **Return:** The tolerable size of the attack $\min\{P, Q\}$.
-

B Proof of Theorem 5.1

Proof. Firstly, we know that the α -Rényi divergence between two Gaussian distributions $\mathcal{N}(0, \sigma^2 I_d)$ and $\mathcal{N}(\mu, \sigma^2 I_d)$ is bounded by $\frac{\alpha \|\mu\|_2^2}{2\sigma^2}$. Thus by the postprocessing property of Rényi divergence we have

$$\begin{aligned} D_\alpha(\tilde{w}(x), \tilde{w}(x')) &= D_\alpha(Z(T(x + z)), Z(T(x' + z))) \leq D_\alpha(x + z, x' + z) \\ &\leq \frac{\alpha \|x - x'\|_F^2}{2\sigma^2} \leq \frac{\alpha R^2}{2\sigma^2}. \end{aligned}$$

Thus, when $\frac{\alpha R^2}{2\sigma^2} \leq \gamma$ it satisfies the utility robustness.

Second, we show it satisfies the prediction robustness. We first recall the following lemma which shows an lower bound between the Rényi divergence of two discrete distributions:

Lemma B.1 (Rényi Divergence Lemma Li et al. (2019)). *Let $P = (p_1, p_2, \dots, p_k)$ and $Q = (q_1, q_2, \dots, q_k)$ be two multinomial distributions. If the indices of the largest probabilities **do not***

match on P and Q , then the Rényi divergence between P and Q , i.e., $D_\alpha(P||Q)^2$, satisfies

$$D_\alpha(P||Q) \geq -\log(1 - p_{(1)} - p_{(2)}) + 2\left(\frac{1}{2}(p_{(1)}^{1-\alpha} + p_{(2)}^{1-\alpha})\right)^{\frac{1}{1-\alpha}}.$$

where $p_{(1)}$ and $p_{(2)}$ refer to the largest and the second largest probabilities in $\{p_i\}$, respectively.

By Lemma B.1 we can see that as long as $D_\alpha(\tilde{w}(x), \tilde{w}(x')) \leq -\log(1 - p_{(1)} - p_{(2)}) + 2\left(\frac{1}{2}(p_{(1)}^{1-\alpha} + p_{(2)}^{1-\alpha})\right)^{\frac{1}{1-\alpha}}$ we must have the prediction robustness. Thus, if $\frac{\alpha R^2}{2\sigma^2} \leq -\log(1 - p_{(1)} - p_{(2)}) + 2\left(\frac{1}{2}(p_{(1)}^{1-\alpha} + p_{(2)}^{1-\alpha})\right)^{\frac{1}{1-\alpha}}$ we have the condition.

Finally we proof the Top- K robustness. The idea of the proof follows Liu et al. (2021). We proof the following lemma first

Lemma B.2. Consider the set of all vectors with unit ℓ_1 -norm in \mathbb{R}^T , \mathcal{Q} . Then we have

$$\begin{aligned} \min_{q \in \mathcal{Q}, V_k(\hat{w}, q) \geq \beta} D_\alpha(\hat{w}, q) &= \frac{\alpha}{\alpha - 1} \ln(2k_0 \left(\sum_{i \in \mathcal{S}} \tilde{w}_i^\alpha\right)^{\frac{1}{\alpha}} \\ &\quad + (2k_0)^{\frac{1}{\alpha}} \sum_{i \notin \mathcal{S}} \tilde{w}_i) - \frac{1}{\alpha - 1} \ln(2k_0), \end{aligned}$$

where $D_\alpha(\hat{w}, q)$ is the α -divergence of the distributions whose probability vectors are \hat{w} and q .

Now we back to the proof, we know that $D_\alpha(x+z, x'+z) \leq \frac{\alpha R^2}{2\sigma^2}$. And $D_\alpha(Z(T(x+z)), Z(T((x'+z))) \leq D_\alpha(x+z, x'+z)$. Thus, if $\frac{\alpha R^2}{2\sigma^2} \leq \frac{\alpha}{\alpha-1} \ln(2k_0 \left(\sum_{i \in \mathcal{S}} \tilde{w}_i^\alpha\right)^{\frac{1}{\alpha}} + (2k_0)^{\frac{1}{\alpha}} \sum_{i \notin \mathcal{S}} \tilde{w}_i) - \frac{1}{\alpha-1} \ln(2k_0)$ we must have $V_k(g(x+z), g(x'+z)) \geq \beta$.

□

Proof of Lemma B.2. We denote $m^T = (m_1, m_2, \dots, m_T)$ and $q^T = (q_1, \dots, q_T)$. W.l.o.g we assume that $m_1 \geq \dots \geq m_T$. Then, to reach the minimum of Rényi divergence we show that the minimizer q must satisfies $q_1 \geq \dots \geq q_{k-k_0-1} \geq q_{k-k_0} = \dots = q_{k+k_0+1} \geq q_{k+k_0+2} \geq q_T$. We need the following statements for the proof.

Lemma B.3. We have the following statements:

1. To reach the minimum, there are exactly k_0 different components in the top- k of \tilde{w} and q .
2. To reach the minimum, q_{k-k_0+1}, \dots, q_k are not in the top- k of q .
3. To reach the minimum, $q_{k+1}, \dots, q_{k+k_0}$ must appear in the top- k of q .
4. Li et al. (2019) To reach the minimum, we must have $q_i \geq q_j$ for all $i \leq j$.

Thus, based on Lemma B.3, we only need to solve the following optimization problem to find a minimizer q :

$$\begin{aligned} \min_{q_1, \dots, q_T} &= \sum_{i=1}^T q_i \left(\frac{\tilde{w}_i}{q_i}\right)^\alpha \\ \text{s.t. } &\sum_{i=1}^T q_i = 1 \\ \text{s.t. } &q_i \leq q_j, i \geq j \\ \text{s.t. } &q_i \geq 0 \\ \text{s.t. } &q_i - q_j = 0, \forall i, j \in \mathcal{S} = \{k - k_0 + 1, \dots, k + k_0\} \end{aligned}$$

²For $\alpha \in (1, \infty)$, $D_\alpha(P||Q)$ is defined as $D_\alpha(P||Q) = \frac{1}{\alpha-1} \log \mathbb{E}_{x \sim Q} \left(\frac{P(x)}{Q(x)}\right)^\alpha$.

Solve the above optimization by using Lagrangian method we can get

$$q_i = \frac{s}{2k_0 s + (2k_0)^{\frac{1}{\alpha}} \sum_{i \notin \mathcal{S}} \tilde{w}_i}, \forall i \in \mathcal{S}, \quad (2)$$

$$q_i = \frac{(2k_0)^{\frac{1}{\alpha}} \tilde{w}_i}{2k_0 s + (2k_0)^{\frac{1}{\alpha}} \sum_{i \notin \mathcal{S}} \tilde{w}_i}, \forall i \notin \mathcal{S} \quad (3)$$

where $s = (\sum_{i \in \mathcal{S}} \tilde{w}_i^\alpha)^{\frac{1}{\alpha}}$. We can get in this case $D_\alpha(\tilde{w}, q) = \frac{\alpha}{\alpha-1} \ln(2k_0 s + (2k_0)^{\frac{1}{\alpha}} \sum_{i \notin \mathcal{S}} \tilde{w}_i) - \frac{1}{\alpha-1} \ln(2k_0)$. □

Proof of Lemma B.3. We first proof the first item:

Assume that i_1, \dots, i_{k_0+j} are the j components in the top-k of \tilde{w} but not in the top-k of q , and i'_1, \dots, i'_{k_0+j} are the components in the top-k of q but not in the top-k of \tilde{w} . Consider we have another vector q^1 with the same value with q while replace $q_{i_{k_0+j}}$ with $q_{i'_{k_0+j}}$. Thus we have

$$\begin{aligned} & e^{(\alpha-1)D_\alpha(\tilde{w}, q^1)} - e^{(\alpha-1)D_\alpha(\tilde{w}, q)} \\ &= \left(\frac{\tilde{w}_{i_{k_0+j}}^\alpha}{q_{i_{k_0+j}}^{\alpha-1}} + \frac{\tilde{w}_{i'_{k_0+j}}^\alpha}{q_{i'_{k_0+j}}^{\alpha-1}} \right) - \left(\frac{\tilde{w}_{i_{k_0+j}}^\alpha}{q_{i_{k_0+j}}^{\alpha-1}} + \frac{\tilde{w}_{i'_{k_0+j}}^\alpha}{q_{i'_{k_0+j}}^{\alpha-1}} \right) \\ &= (\tilde{w}_{i_{k_0+j}}^\alpha - \tilde{w}_{i'_{k_0+j}}^\alpha) \left(\frac{1}{q_{i'_{k_0+j}}^{\alpha-1}} - \frac{1}{q_{i_{k_0+j}}^{\alpha-1}} \right) < 0, \end{aligned}$$

since $\tilde{w}_{i_{k_0+j}} \geq \tilde{w}_{i'_{k_0+j}}$ and $q_{i'_{k_0+j}} \geq q_{i_{k_0+j}}$. Thus, we know reducing the number of misplacement in top-k can reduce the value $D_\alpha(\tilde{w}, q)$ which contradict to q achieves the minimal. Thus we must have $j = 0$.

We then proof the second statement.

Assume that i_1, \dots, i_{k_0} are the k_0 components in the top-k of \tilde{w} but not in the top-k of q , and i'_1, \dots, i'_{k_0} are the components in the top-k of q but not in the top-k of \tilde{w} . Consider we have another unit ℓ_1 -norm vector q^2 with the same value with q while q_{i_j} is replaced by $q_{j'}$ where $\tilde{w}_{j'} \geq \tilde{w}_{i_j}$ and j' is in the top-k component of q (there must exists such index j'). Now we can see that $q_{j'}^2$ is no longer a top-k component of q^2 and $q_{i_j}^2$ is a top-k component. Thus we have

$$\begin{aligned} & e^{(\alpha-1)D_\alpha(\tilde{w}, q^2)} - e^{(\alpha-1)D_\alpha(\tilde{w}, q)} \\ &= \left(\frac{\tilde{w}_{i_j}^\alpha}{q_{j'}^{\alpha-1}} + \frac{\tilde{w}_{j'}^\alpha}{q_{i_j}^{\alpha-1}} \right) - \left(\frac{\tilde{w}_{i_j}^\alpha}{q_{i_j}^{\alpha-1}} + \frac{\tilde{w}_{j'}^\alpha}{q_{j'}^{\alpha-1}} \right) \\ &= (\tilde{w}_{i_j}^\alpha - \tilde{w}_{j'}^\alpha) \left(\frac{1}{q_{j'}^{\alpha-1}} - \frac{1}{q_{i_j}^{\alpha-1}} \right) \geq 0. \end{aligned}$$

Now we back to the proof of the statement. We first proof q_k is not in the top-k of q . If not, that is $k \notin \{i_1, \dots, i_{k_0}\}$ and all $i_j < k$. Then we can always find an $i_j < k$ such that $\tilde{w}_k \leq \tilde{w}_{i_j}$, we can find a vector \tilde{q} by replacing q_{i_j} with q_k . And we can see that $D_\alpha(\tilde{w}, \tilde{q}) - D_\alpha(\tilde{w}, q) \leq 0$, which contradict to that q is the minimizer.

We then proof q_{k-1} is not in the top-k of q . If not we can construct \tilde{q} by replacing q_k with q_{k-1} . Since q_k is not in top-k and $\tilde{w}_k \leq \tilde{w}_{k-1}$. By the previous statement we have $D_\alpha(\tilde{w}, \tilde{q}) - D_\alpha(\tilde{w}, q) \leq 0$, which contradict to that q is the minimizer. Thus, q_{k-1} is not in the top-k of q . We can thus use induction to proof statement 2.

Finally we proof statement 3. We can easily show that $q_i \geq q_{k+1}$ for $i \leq k$, and $q_i \leq q_{k+1}$ for $i \geq k+2$. Thus, q_1, \dots, q_k are greater than the left entries. Since by Statement 2 we have q_{k-k_0}, \dots, q_k are not top k . Thus we must have $q_{k+1}, \dots, q_{k+k_0}$ must be top-k of q . □

C Proof of Theorem 5.2

Proof. For simplicity in the following we think the data x as a d -dimensional vector and thus the Frobenious norm now becomes to the ℓ_2 -norm of the vector and the max norm becomes to the ℓ_∞ -norm of the vector.

We first show that, in order to prove Theorem 5.2, we only need to prove Theorem C.1. Then we show that, to prove Theorem C.1, we only need to prove Theorem C.2. Finally, we give a formal proof of Theorem C.2.

Theorem C.1. *For any $\gamma \leq O(1)$, if a randomized (smoothing) mechanism $\mathcal{M}(x) = x + z : \{0, \frac{R}{2\sqrt{d}}\}^d \mapsto \mathbb{R}^d$ that $D_\alpha(\mathcal{M}(x), \mathcal{M}(x')) \leq \gamma$ for all $\|x - x'\|_2 \leq R$. Moreover, if we have for any $x \in \{0, \frac{R}{2\sqrt{d}}\}^d$,*

$$\mathbb{E}[\|z\|_\infty] = \mathbb{E}[\|\mathcal{M}(x) - x\|_\infty] \leq \tau$$

for some $\tau \leq O(1)$. Then it must be true that $\tau \geq \Omega(\frac{\sqrt{\alpha}R}{\sqrt{\gamma}})$.

For any $\mathcal{M}(x) = x + z : \mathbb{R}^d \mapsto \mathbb{R}^d$, in Theorem C.1, we only consider the expected ℓ_∞ -norm of the noise added by $\mathcal{M}(x)$ on $x \in \{0, \frac{R}{2\sqrt{d}}\}^d$. Thus, the τ in Theorem C.1 should be less than or equal to the τ in Theorem 5.2 (on $x \in \mathbb{R}^d$). Therefore, the lower bound for the τ in Theorem C.1 (i.e., $\Omega(\frac{\sqrt{\alpha}R}{\sqrt{\gamma}})$) is also a lower bound for the τ in Theorem 5.2. That is to say, if Theorem C.1 holds, then Theorem 5.2 also holds true.

Next, we show that if Theorem C.2 holds, then Theorem C.1 also holds.

Theorem C.2. *For any $\gamma \leq O(1)$, if a randomized (smoothing) mechanism $\mathcal{M}(x)^3 : \{0, \frac{R}{2\sqrt{d}}\}^d \mapsto [0, \frac{R}{2\sqrt{d}}]^d$ that $D_\alpha(\mathcal{M}(x), \mathcal{M}(x')) \leq \gamma$ for all $\|x - x'\|_2 \leq R$. Moreover, if for any $x \in \{0, \frac{R}{2\sqrt{d}}\}^d$*

$$\mathbb{E}[\|z\|_\infty] = \mathbb{E}[\|\mathcal{M}(x) - x\|_\infty] \leq \tau$$

for some $\tau \leq O(1)$. Then it must be true that $\tau \geq \Omega(\frac{\sqrt{\alpha}R}{\sqrt{\gamma}})$.

Proof of Theorem C.1 For any $\mathcal{M}(x) = x + z : \{0, \frac{R}{2\sqrt{d}}\}^d \mapsto \mathbb{R}^d$ considered in Theorem C.1 that $D_\alpha(\mathcal{M}(x), \mathcal{M}(x')) \leq \gamma$ for all $\|x - x'\|_2 \leq R$, there randomized mechanism $\mathcal{M}''(x) : \{0, \frac{R}{2\sqrt{d}}\}^d \mapsto [0, \frac{R}{2\sqrt{d}}]^d$ considered in Theorem C.2 such that for all $x \in \{0, \frac{R}{2\sqrt{d}}\}^d$

$$\mathbb{E}[\|\mathcal{M}''(x) - x\|_\infty] \leq \mathbb{E}[\|\mathcal{M}(x) - x\|_\infty].$$

To prove the above statement, we first let $a = \frac{R}{2\sqrt{d}}$ and $\mathcal{M}'(x) = \min\{\mathcal{M}(x), a\}$, where \min is a coordinate-wise operator. Now we fix the randomness of $\mathcal{M}(x)$ (that is $\mathcal{M}(x)$ is deterministic), and we assume that $\|\mathcal{M}(x) - x\|_\infty = |\mathcal{M}_j(x) - x_j|$, $\|\mathcal{M}'(x) - x\|_\infty = |\mathcal{M}'_i(x) - x_i|$. If $\mathcal{M}_i(x) < a$, then by the definitions, we have $|\mathcal{M}'(x) - x|_\infty = |\mathcal{M}'_i(x) - x_i| = |\mathcal{M}_i(x) - x_i| \leq \|\mathcal{M}(x) - x\|_\infty$. If $\mathcal{M}_i(x) \geq a$, then we have $|\mathcal{M}'_i(x) - x_i| = |a - x_i|$. Since $x_i \in \{0, a\}$ and $\mathcal{M}_i(x) \geq a$, $|\mathcal{M}_i(x) - x_i| \geq |a - x_i|$. $\|\mathcal{M}(x) - x\|_\infty \geq |\mathcal{M}_i(x) - x_i| \geq |a - x_i|$. Thus, $\mathbb{E}[\|\mathcal{M}'(x) - x\|_\infty] \leq \mathbb{E}[\|\mathcal{M}(x) - x\|_\infty]$.

Then, we let $\mathcal{M}''(x) = \max\{\mathcal{M}'(x), 0\}$ where \max is also a coordinate-wise operator. We can use a similar method to prove that $\mathbb{E}[\|\mathcal{M}''(x) - x\|_\infty] \leq \mathbb{E}[\|\mathcal{M}'(x) - x\|_\infty] \leq \mathbb{E}[\|\mathcal{M}(x) - x\|_\infty]$. Also, we can see that $\mathcal{M}''(x) = \max\{0, \min\{\mathcal{M}(x), a\}\}$, which means \mathcal{M}'' satisfies $D_\alpha(\mathcal{M}''(x), \mathcal{M}''(x')) \leq \gamma$ for all $\|x - x'\|_2 \leq R$ due to the postprocessing property.

Since $\mathbb{E}[\|\mathcal{M}''(x) - x\|_\infty] \leq \mathbb{E}[\|\mathcal{M}(x) - x\|_\infty]$, and $\mathcal{M}''(x)$ is a randomized mechanism satisfying the conditions in Theorem C.2, the τ in Theorem C.2 should be less than or equal to the τ in Theorem C.1. Therefore, the lower bound for the τ in Theorem C.2 is also a lower bound for the τ in Theorem C.1. That is to say, if Theorem C.2 holds, then Theorem C.1 also holds.

Finally, we give a proof of Theorem C.2. Before that we need to review some definitions of Differential Privacy Dwork et al. (2006).

³This mechanism might not be simply $x + z$ since it must involve operations to clip the output into $[0, \frac{R}{2\sqrt{d}}]^d$

Definition C.3. Given a data universe X , we say that two datasets $D, D' \subset X$ are neighbors if they differ by only one entry, which is denoted by $D \sim D'$. A randomized algorithm \mathcal{M} is (ϵ, δ) -differentially private (DP) if for all neighboring datasets D, D' and all events S the following holds

$$P(\mathcal{M}(D) \in S) \leq e^\epsilon P(\mathcal{M}(D') \in S) + \delta.$$

Definition C.4. A randomized algorithm \mathcal{M} is (α, ϵ) -Rényi differentially private (DP) if for all neighboring datasets D, D' the following holds

$$D_\alpha(\mathcal{M}(D) \| \mathcal{M}(D')) \leq \epsilon.$$

Lemma C.5 (From RDP to DP Mironov (2017)). *If a mechanism is (α, ϵ) -RDP, then it also satisfies $(\epsilon + \frac{\log \frac{1}{\delta}}{\alpha-1}, \delta)$ -DP.*

Proof of Theorem C.2 Since \mathcal{M} satisfies $D_\alpha(\mathcal{M}(x), \mathcal{M}(x')) \leq \gamma$ for all $\|x - x'\|_2 \leq R$ on $\{0, \frac{r}{2\sqrt{d}}\}^d$, and for any $x_i, x_j \in \{0, \frac{R}{2\sqrt{d}}\}^d$, $\|x_i - x_j\|_2 \leq R$ (i.e., $x_j \in \mathbb{B}_2(x_i, R)$), we can see \mathcal{M} is (α, γ) -RDP on $\{0, \frac{r}{2\sqrt{d}}\}^d$. Thus by Lemma C.5 we can see \mathcal{M} is $(\gamma + 2\frac{\log \frac{1}{\delta}}{\alpha-1}, \delta)$ -DP on $\{0, \frac{r}{2\sqrt{d}}\}^d$.

Then let us take use of the above condition by connecting the lower bound of the sample complexity to estimate one-way marginals (i.e., mean estimation) for DP mechanisms with the lower bound studied in Theorem C.2. Suppose an n -size dataset $X \in \mathbb{R}^{n \times d}$, the one-way marginal is $h(D) = \frac{1}{n} \sum_{i=1}^n X_i$, where X_i is the i -th row of X . In particular, when $n = 1$, one-way marginal is just the data point itself, and thus, the condition in Theorem C.2 can be rewritten as

$$\mathbb{E}[\|\mathcal{M}(D) - h(D)\|_\infty] \leq \alpha. \quad (4)$$

Based on this connection, we first prove the case where $r = 2\sqrt{d}$, and then generalize it to any r . For $r = 2\sqrt{d}$, the conclusion reduces to $\tau \geq \Omega(\sqrt{\frac{d}{\epsilon}})$. To prove this, we employ the following lemma, which provides a one-way margin estimation for all DP mechanisms.

Lemma C.6 (Theorem 1.1 in Steinke and Ullman (2016)). *For any $\epsilon \leq O(1)$, every $2^{-\Omega(n)} \leq \delta \leq \frac{1}{n^{1+\Omega(1)}}$ and every $\alpha \leq \frac{1}{10}$, if $\mathcal{M} : (\{0, 1\}^d)^n \mapsto [0, 1]^d$ is (ϵ, δ) -DP and $\mathbb{E}[\|\mathcal{M}(D) - h(D)\|_\infty] \leq \tau$, then we have $n \geq \Omega(\frac{\sqrt{d \log \frac{1}{\delta}}}{\epsilon \tau})$.*

Setting $n = 1, \epsilon = \gamma + 2\frac{\log \frac{1}{\delta}}{\alpha-1}$ in Lemma C.6, we can see that if $\mathbb{E}[\|\mathcal{M}(x) - x\|_\infty] \leq \tau$, then we must have

$$1 \geq \Omega\left(\frac{\sqrt{d \log \frac{1}{\delta}}}{(\gamma + 2\frac{\log \frac{1}{\delta}}{\alpha-1})\tau}\right) \geq \Omega\left(\frac{\sqrt{\alpha} \sqrt{d}}{\sqrt{\gamma} \tau}\right),$$

where the last inequality holds if α is sufficiently large and γ is sufficiently small. Therefore, we have the following theorem,

Theorem C.7. *For all \mathcal{M} satisfies $D_\alpha(\mathcal{M}(x), \mathcal{M}(x')) \leq \gamma$ for all $\|x - x'\|_2 \leq 2\sqrt{d}$ on $\{0, 1\}^d$ such that*

$$\mathbb{E}[\|\mathcal{M}(x) - x\|_\infty] \leq \tau, \quad (5)$$

for some $\tau \leq O(1)$. Then $\tau \geq \Omega(\frac{\sqrt{\alpha d}}{\sqrt{\gamma}})$.

Apparently, Theorem C.7 is special case of Theorem C.2 where $R = 2\sqrt{d}$. Now we come back to the proof for any $\mathcal{M}(x) : \{0, \frac{r}{2\sqrt{d}}\}^d \mapsto [0, \frac{r}{2\sqrt{d}}]^d$ satisfies $D_\alpha(\mathcal{M}(x), \mathcal{M}(x')) \leq \gamma$ for all $\|x - x'\|_2 \leq R$. We substitute $\frac{2\sqrt{d}}{R}x$ with $\tilde{x} \in \{0, 1\}^d$ and construct $\tilde{\mathcal{M}}$ as $\tilde{\mathcal{M}}(\tilde{x}) = \frac{2\sqrt{d}}{R}\mathcal{M}(x) \in [0, 1]^d$. Since $\mathcal{M}(x)$ satisfies

$$\mathbb{E}[\|\mathcal{M}(x) - x\|_\infty] \leq \tau,$$

then we have

$$\mathbb{E}[\|\tilde{\mathcal{M}}(\tilde{x}) - \tilde{x}\|_\infty] = \mathbb{E}[\|\frac{2\sqrt{d}}{R}\mathcal{M}(x) - \frac{2\sqrt{d}}{R}x\|_\infty] \leq \frac{2\sqrt{d}}{R}\alpha.$$

By the postprocessing property of Rényi divergence we can see $D_\alpha(\tilde{\mathcal{M}}(x), \tilde{\mathcal{M}}(x')) \leq \gamma$ for all $\|x - x'\|_2 \leq 2\sqrt{d}$.

Considering $\tilde{\mathcal{M}} : \{0, 1\}^d \mapsto [0, 1]^d$ in Theorem C.7 with $\tau = \frac{2\sqrt{d}}{r}\tau \leq O(1)$ (because $\mathbb{E}[\|\tilde{\mathcal{M}}(\tilde{x}) - \tilde{x}\|_\infty] \leq \frac{2\sqrt{d}}{R}\tau$), we have

$$\frac{2\sqrt{d}}{R}\tau \geq \Omega\left(\frac{\sqrt{\alpha d}}{\sqrt{\gamma}}\right). \quad (6)$$

Therefore, Theorem C.2 holds true, thus, Theorem C.1 also holds true, and Theorem 5.2 is proved. \square

D Proof of Theorem 5.3

Proof. We can see the dataset as a d -dimensional vector by unfolding it. Thus, now the max norm of a matrix becomes to the ℓ_∞ -norm of a vector. Firstly, we know that the α -Rényi divergence between two Gaussian distributions $\mathcal{N}(0, \sigma^2 I_d)$ and $\mathcal{N}(\mu, \sigma^2 I_d)$ is bounded by $\frac{\alpha\|\mu\|_2^2}{2\sigma^2} \leq \frac{\alpha d R^2}{2\sigma^2}$. Thus by the postprocessing property of Rényi divergence we have

$$\begin{aligned} D_\alpha(\tilde{w}(x), \tilde{w}(x')) &= D_\alpha(Z(T(x+z)), Z(T(x')))) \leq D_\alpha(x+z, x'+z) \\ &\leq \frac{\alpha\|x - x'\|_F^2}{2\sigma^2} \leq \frac{\alpha d R^2}{2\sigma^2}. \end{aligned}$$

Thus, when $\frac{d\alpha R^2}{2\sigma^2} \leq \gamma$ it satisfies the utility robustness. For the prediction and top- k robustness we can use the similar proof as in Theorem 5.1. We omit it here for simplicity. \square

E Proof of Theorem 5.4

Proof. Similar to the proof of Theorem 5.2, in order to prove Theorem 5.4, we only need to prove the following theorem:

Theorem E.1. *If there is a randomized (smoothing) mechanism $\mathcal{M}(x) : \{0, \frac{r}{2}\}^d \mapsto [0, \frac{r}{2}]^d$ such that $D_\alpha(\mathcal{M}(x), \mathcal{M}(x')) \leq \gamma$ for all $\|x - x'\|_\infty \leq R$ for any $x \in \{0, \frac{r}{2}\}^d$, the following holds*

$$\mathbb{E}[\|z\|_\infty] = \mathbb{E}[\|\mathcal{M}(x) - x\|_\infty] \leq \gamma$$

for some $\gamma \leq O(1)$. Then it must be true that $\gamma \geq \Omega(\frac{\sqrt{\alpha d}}{\sqrt{\gamma}})$.

Since \mathcal{M} satisfies $D_\alpha(\mathcal{M}(x), \mathcal{M}(x')) \leq \gamma$ for all $\|x - x'\|_\infty \leq R$ on $\{0, \frac{r}{2}\}^d$, and for any $x_i, x_j \in \{0, \frac{r}{2}\}^d$, $\|x_i - x_j\|_2 \leq R$ (i.e., $x_j \in \mathbb{B}_2(x_i, R)$), we can see \mathcal{M} is (α, γ) -RDP on $\{0, \frac{r}{2}\}^d$. Thus by Lemma C.5 we can see \mathcal{M} is $(\gamma + 2\frac{\log \frac{1}{\alpha}}{\alpha-1}, \delta)$ -DP on $\{0, \frac{r}{2}\}^d$.

We first consider the case where $r = 2$. By setting $n = 1$ and $\gamma = \gamma + 2\frac{\log \frac{1}{\alpha}}{\alpha-1}$ in Lemma C.6, we have a similar result as in Theorem C.7:

Theorem E.2. *For all \mathcal{M} satisfies $D_\alpha(\mathcal{M}(x), \mathcal{M}(x')) \leq \gamma$ for all $\|x - x'\|_\infty \leq 2$ on $\{0, 1\}^d$ such that*

$$\mathbb{E}[\|\mathcal{M}(x) - x\|_\infty] \leq \tau, \quad (7)$$

for some $\tau \leq O(1)$. Then $\tau \geq \Omega(\frac{\sqrt{\alpha d}}{\sqrt{\gamma}})$.

For general R , similar to the proof of Theorem C.2, we substitute $\frac{2}{R}x$ with $\tilde{x} \in \{0, 1\}^d$ and construct $\tilde{\mathcal{M}}$ as $\tilde{\mathcal{M}}(\tilde{x}) = \frac{2}{R}\mathcal{M}(x) \in [0, 1]^d$. Since $\mathcal{M}(x)$ satisfies

$$\mathbb{E}[\|\mathcal{M}(x) - x\|_\infty] \leq \alpha,$$

then we have

$$\mathbb{E}[\|\tilde{\mathcal{M}}(\tilde{x}) - \tilde{x}\|_\infty] = \mathbb{E}[\|\frac{2}{R}\mathcal{M}(x) - \frac{2}{R}x\|_\infty] \leq \frac{2}{R}\alpha.$$

Also, $\tilde{\mathcal{M}} : \{0, 1\}^d \mapsto [0, 1]^d$ satisfies $D_\alpha(\tilde{\mathcal{M}}(x), \tilde{\mathcal{M}}(x')) \leq \gamma$ for all $\|x - x'\|_\infty \leq R$ on $\{0, \frac{R}{2}\}^d$. Thus by Theorem E.2 with $\alpha = \frac{2}{R}\alpha$ we have

$$\alpha \geq \Omega\left(\frac{R\sqrt{\alpha d}}{\sqrt{\gamma}}\right),$$

thus we have Theorem E.1. \square

F Baseline Methods

Five baseline methods are considered in this paper. The implementation and parameter setting of each method is based on the corresponding official code. Note that in this paper, we did not involve compression with Shapely-value methods Lundberg and Lee (2017) due to the large computational complexity and sub-optimal performance Chen et al. (2018).

1. **Raw Attention Vaswani et al. (2017).** It is common practice to consider the raw attention value as a relevancy score for a single attention layer in both visual and language domains Xu et al. (2015). However, for the case of multiple layers, the attention score in deeper layers may be unreliable for explaining the importance of each token due to the token mixing property Lee-Thorp et al. (2021) of the self-attention mechanism. Based on observations in Chefer et al. (2021), we consider the raw attention in the first layer since they are more faithful in explanation compared to deeper layers.
2. **Rollout Abnar and Zuidema (2020).** To compute the attention weights from positions in layer l_i to positions in layer l_j in a Transformer with L layers, we multiply the attention weights matrices in all the layers below the layer l_i . If $i > j$, we multiply by the attention weights matrix in the layer l_{i-1} , and if $i = j$, we do not multiply by any additional matrices. This process can be represented by the following equation:

$$\tilde{A}(l_i) = \begin{cases} A(l_i)\tilde{A}(l_{i-1}) & \text{if } i > j \\ A(l_i) & \text{if } i = j \end{cases}$$

3. **GradCAM Selvaraju et al. (2017).** The main motivation of the Class Activation Mapping (CAM) approach is to obtain a weighted map based on the feature channels in one layer. The derived map can explain the importance of each pixel of the input image based on the intuition that non-related features are filtered in the channels of the deep layer. GradCAM Selvaraju et al. (2017) proposes to leverage the gradient information by globally averaging the gradient score as the weight. To be more specific, the weight of channel k with respect to class c is calculated using

$$\alpha_k^c = \frac{1}{Z} \sum_i \sum_j \frac{\partial y^c}{\partial A_{ij}^k},$$

where α_k^c is the attention weight for feature map k of the final convolutional layer, for class c . y^c is the output class score for class c , and A_{ij}^k is the activation at location (i, j) in feature map k . The summation over i and j indicates that the gradient is computed over all locations in the feature map. The normalization factor Z is the sum of all the attention weights for the feature maps in the final convolutional layer.

4. **LRP Bach et al. (2015).** Layer-wise Relevance Propagation (LRP) method propagates relevance from the predicated score in the final layer to the input image based on the Deep Taylor Decomposition (DTD) Montavon et al. (2017) framework. Specifically, to compute the relevance of each neuron in the network, we iteratively perform backward propagation using the following equation:

$$R_j = \sum_k \frac{u_j w_{jk}}{\sum_j a_j w_{jk} + \epsilon \cdot \text{sign}(a_j w_{jk})} R_k,$$

where R_j and R_k are the relevance scores of neurons j and k , respectively, in consecutive layers of the network. a represents the activation of neuron j , $w_{j,k}$ is the weight between neurons j and k , and ϵ is a small constant used as a stabilizer to prevent numerical degeneration. For more information on this technique, please see the original paper.

5. **VTA Chefer et al. (2021).** Vanilla Trans. Att. (VTA) uses a LRP-based relevance score to evaluate the importance of each attention head in each layer. These scores are then integrated throughout the attention graph by combining relevancy and gradient information in an iterative process that eliminates negative values.

G Implementation details

Diffusion Denoiser Implementation. For COCO and CitySpace, we trained the diffusion models from scratch following Ho et al. (2020). For ImageNet, we leverage the pre-trained diffusion model released in the guided-diffusion. Specifically, the 256x256_diffusion_uncond is used as a denoiser. To resolve the size mismatch, we resize the images each time of their inputs and outputs from the diffusion model. The diffusion model we adopted uses a linear noise schedule with $\beta_1 = 0.0001$ and $\beta_N = 0.02$. The sampling steps N are set to 1000. We clip the optimal t^* when it falls outside the range of $[0, N - 1]$.

Max-fuse with lowest pixels drop. After obtaining explanation maps with a number of sampled noisy images, instead of fusing these maps with *mean* operation, we leverage the approach of max fusing with the lowest pixels drop following Jacobgil. Specifically, we drop the lowest 10% unimportant pixels for each map and apply element-wise maximum on the set of modified maps. The element of the final map is re-scaled to $[0, 1]$ using min-max normalization.

Model Training Details. We use the pre-trained backbones in the `timm` library for feature extractor of classification and segmentation. As for different ViT, we both leverage the base version with a patch size of 16 and an image size of 224. For the downstream dataset, we then fine-tuned these models using the Adam optimizer with a learning rate of 0.001 for a total of 50 epochs, with a batch size of 128. To prevent overfitting, we implemented early stopping with a criterion of 20 epochs. For data augmentation, we follow the common practice: `Resize(256) → CenterCrop(224) → ToTensor → Normalization`. And the mean and stand deviation of normalization are both $[0.5, 0.5, 0.5]$.

Adversarial Perturbation. The perturbation radius is denoted by ρ_u and is set to $8/255$ unless otherwise stated. For CIFAR-10, ImageNet, and COCO, the step size is set to $\rho_u/5$, and the total number of steps is set to 10. For the Cityscape dataset, the step size was set to $\rho_u/125$, and the total number of steps was set to 250.

H More Results

In this section, we provide more results to demonstrate the performance of our methods in terms of both model prediction and explainability. First, we aim to evaluate whether our method will affect utility when no attack is presented. We evaluate this on the ImageNet classification dataset using three different kinds of model architectures. Then we ablate the component proposed in our method to study their individual contributions.

Clean Utility. As we can see from Table 4, our method outperforms the Vanilla approach under a relatively small smoothing radius, $\delta = 2/255$. This result suggests that our method is able to enhance the classification utility with appropriate δ . However, we also find that, as δ increases to $\delta = 5/255$, there is a slight performance drop. And as the δ increases to $\delta = 10/255$, the testing accuracy drops more, which indicates the necessity of choosing the right δ . Since too large δ might lead to the smoothed images being overwhelmed with noise, which will lead to lower classification confidence. In a word, the results show that our method can even improve clean utility with appropriate small δ .

More Experiments of Attacks. We test more adversarial attacks, including PGD, FGSM and AutoAttack in Tab. 5. The results show that our FViT performs well in explanation for the perturbed image across different adversarial attacks and the AutoAttack is the strongest one in degrading the explanation faithfulness among considered baselines. Moreover, our FViT still successfully explains the correct region for the given class. We define a faithfulness score. The details are as follows.

Given the heat map M_{gt} yield on a clean image and perturbed one M_p on a poisoned image, we define faithfulness score S_{Faith} as the reciprocal to the average of the absolute difference between the two heat maps:

$$S_{Faith} = \frac{N}{\sum |M_{gt} - M_p| + \epsilon}, \quad (8)$$

Method	δ	Model		
		ViT	DeiT	Swin
Vanilla	-	85.22	85.80	86.40
Ours	2/255	86.35	86.50	87.20
	5/255	84.83	84.51	85.84
	10/255	79.59	80.89	81.25

Table 4: The testing accuracy of our method and vanilla approach on ImageNet using three different ViT-based models under no attack.


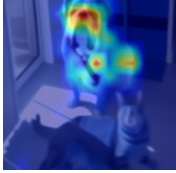
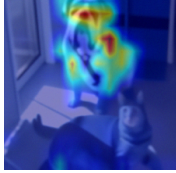
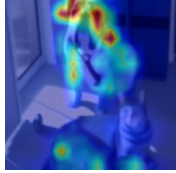
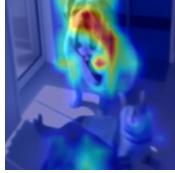
Input	Clean	PGD	FGSM	AutoAttack
				
S_{Faith}	-	4.60	4.45	4.22

Table 5: Faithfulness score S_{Faith} and visualization results of FViT under additional adversarial attack methods with ℓ_∞ -norm threat model and $\rho_u = \frac{8}{255}$. S_{Faith} is reciprocal to the average of the absolute difference between the ground-truth heat map and the predicted one. The higher the score, the more faithful the explanation.

where N is the pixel number and $\epsilon = 0.01$ is a small constant for numerical stability.

Results of ℓ_2 -norm. Mathematically, with the same noise level, ℓ_∞ -norm ball B_∞ is a superset of the ℓ_2 -norm ball B_2 . Thus, it will lead to more powerful attacks. Thus, by showing the effectiveness under ℓ_∞ -norm threat model, we can also bound the performance of FViT under ℓ_2 -norm threat model. We additionally present more results in Tab. 6, which demonstrates this statement since the faithfulness score yield from ℓ_2 -norm threat model is consistently higher than that from ℓ_∞ -norm threat model.

Ablation Study. As shown in Table 7, it suggests that our method outperforms all other baselines on all three datasets under adversarial attacks with different budgets. In particular, On the ImageNet dataset, the ViT model with our method has the highest pixel accuracy at 64%, while the DeiT model with our method had the highest mIoU at 46%. On the Cityscape dataset, the ViT model with Ours had the highest mIoU at 59%. On the COCO dataset, the ViT model with Ours had the highest pixel accuracy at 74% and the highest mIoU at 76%. Moreover, we visualized the ablated version of our method in Figure 8. Overall, our method consistently outperforms all other methods, indicating its superiority in accuracy and robustness.

Norm type	2/255	4/255	6/255	8/255	10/255
ℓ_2	29.16	12.63	10.56	5.62	6.30
ℓ_∞	3.27	11.90	8.79	4.74	4.70

Table 6: Faithfulness score of FViT under ℓ_∞ and ℓ_2 -norm.

Noise Radius	Model	Method	ImageNet				Cityscape				COCO			
			Cla. Acc. (%)	Pix. Acc. (%)	mIoU	mAP	Cla. Acc. (%)	Pix. Acc. (%)	mIoU	mAP	Cla. Acc. (%)	Pix. Acc. (%)	mIoU	mAP
$\rho_u = 9/255$	ViT	Raw Attention	0.6	0.5	0.42	0.77	0.66	0.62	0.46	0.75	0.78	0.65	0.63	0.81
		Rollout	0.72	0.56	0.42	0.76	0.79	0.55	0.51	0.76	0.82	0.64	0.53	0.85
		GradCAM	0.64	0.49	0.5	0.78	0.79	0.64	0.5	0.75	0.74	0.78	0.67	0.91
		LRP	0.7	0.54	0.43	0.78	0.68	0.68	0.52	0.86	0.82	0.69	0.7	0.81
		VTA	0.64	0.56	0.43	0.77	0.7	0.74	0.58	0.89	0.8	0.82	0.67	0.88
		Ours	0.69	0.64	0.48	0.73	0.74	0.71	0.59	0.9	0.88	0.74	0.76	0.97
	DeiT	Raw Attention	0.63	0.6	0.42	0.68	0.75	0.56	0.49	0.71	0.83	0.64	0.57	0.79
		Rollout	0.7	0.57	0.38	0.66	0.69	0.64	0.53	0.76	0.82	0.76	0.57	0.76
		GradCAM	0.67	0.52	0.46	0.81	0.81	0.66	0.55	0.83	0.76	0.71	0.57	0.91
		LRP	0.63	0.63	0.46	0.78	0.81	0.66	0.63	0.79	0.78	0.73	0.66	0.86
		VTA	0.77	0.68	0.54	0.72	0.71	0.71	0.58	0.79	0.82	0.71	0.61	0.86
		Ours	0.8	0.64	0.5	0.81	0.83	0.72	0.67	0.83	0.81	0.72	0.72	0.84
	Swin	Raw Attention	0.65	0.49	0.41	0.76	0.69	0.67	0.44	0.79	0.85	0.72	0.58	0.82
		Rollout	0.62	0.56	0.4	0.81	0.72	0.56	0.52	0.84	0.76	0.69	0.62	0.81
		GradCAM	0.77	0.58	0.4	0.8	0.68	0.68	0.51	0.88	0.87	0.76	0.65	0.86
		LRP	0.67	0.58	0.48	0.74	0.72	0.63	0.52	0.84	0.84	0.79	0.66	0.82
		VTA	0.7	0.59	0.56	0.83	0.85	0.65	0.62	0.88	0.87	0.74	0.72	0.83
		Ours	0.78	0.63	0.49	0.9	0.74	0.78	0.56	0.81	0.86	0.74	0.75	0.93
$\rho_u = 10/255$	ViT	Raw Attention	0.57	0.38	0.34	0.53	0.57	0.46	0.38	0.67	0.74	0.62	0.45	0.66
		Rollout	0.58	0.43	0.38	0.67	0.6	0.55	0.36	0.7	0.66	0.6	0.48	0.69
		GradCAM	0.52	0.39	0.3	0.6	0.57	0.46	0.46	0.63	0.65	0.63	0.45	0.8
		LRP	0.62	0.5	0.38	0.6	0.66	0.57	0.51	0.77	0.65	0.57	0.55	0.71
		VTA	0.52	0.5	0.34	0.68	0.63	0.6	0.46	0.75	0.7	0.69	0.57	0.75
		Ours	0.59	0.54	0.36	0.78	0.74	0.59	0.45	0.72	0.76	0.73	0.63	0.74
	DeiT	Raw Attention	0.53	0.46	0.25	0.62	0.55	0.5	0.39	0.6	0.68	0.63	0.44	0.75
		Rollout	0.6	0.42	0.33	0.66	0.67	0.5	0.44	0.63	0.73	0.55	0.47	0.72
		GradCAM	0.64	0.52	0.37	0.69	0.63	0.54	0.46	0.75	0.67	0.58	0.54	0.72
		LRP	0.65	0.55	0.4	0.73	0.58	0.51	0.53	0.66	0.74	0.65	0.52	0.74
		VTA	0.58	0.54	0.42	0.66	0.64	0.61	0.44	0.68	0.69	0.59	0.5	0.75
		Ours	0.65	0.48	0.47	0.73	0.69	0.66	0.49	0.85	0.76	0.72	0.51	0.85
	Swin	Raw Attention	0.6	0.41	0.3	0.55	0.7	0.54	0.37	0.64	0.63	0.65	0.47	0.72
		Rollout	0.57	0.43	0.36	0.66	0.63	0.51	0.47	0.64	0.64	0.66	0.49	0.7
		GradCAM	0.6	0.47	0.31	0.58	0.58	0.54	0.5	0.67	0.7	0.68	0.48	0.76
		LRP	0.53	0.53	0.32	0.63	0.67	0.6	0.52	0.69	0.72	0.64	0.59	0.84
		VTA	0.59	0.6	0.48	0.68	0.75	0.54	0.51	0.73	0.71	0.61	0.63	0.74
		Ours	0.63	0.54	0.41	0.77	0.78	0.63	0.49	0.79	0.7	0.65	0.62	0.83

Table 7: Comparison of different explanation methods on multiple datasets using ViT, DeiT, and Swin models

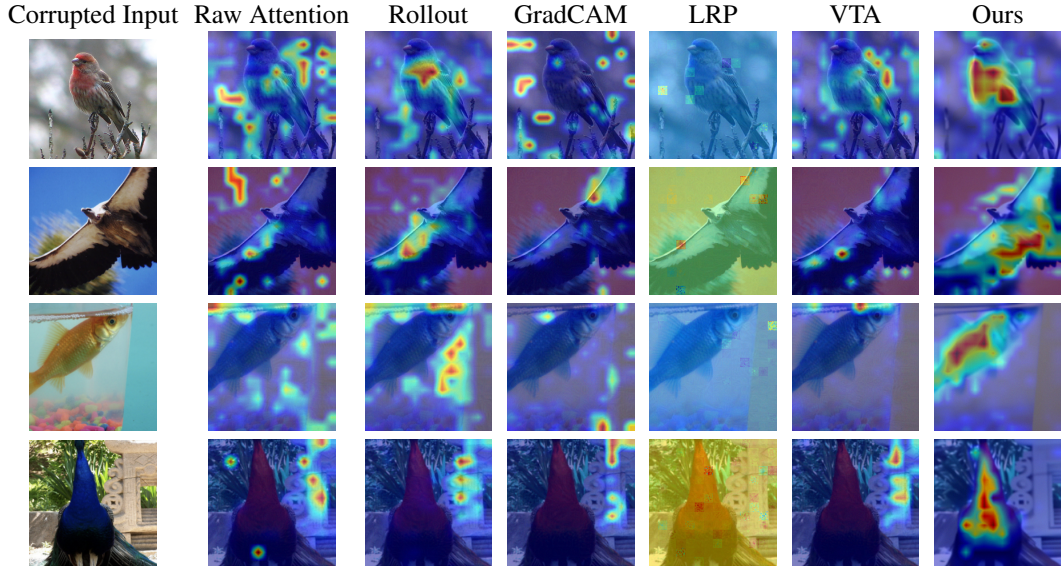


Figure 4: Visualization results of the attention map on corrupted input for different methods.

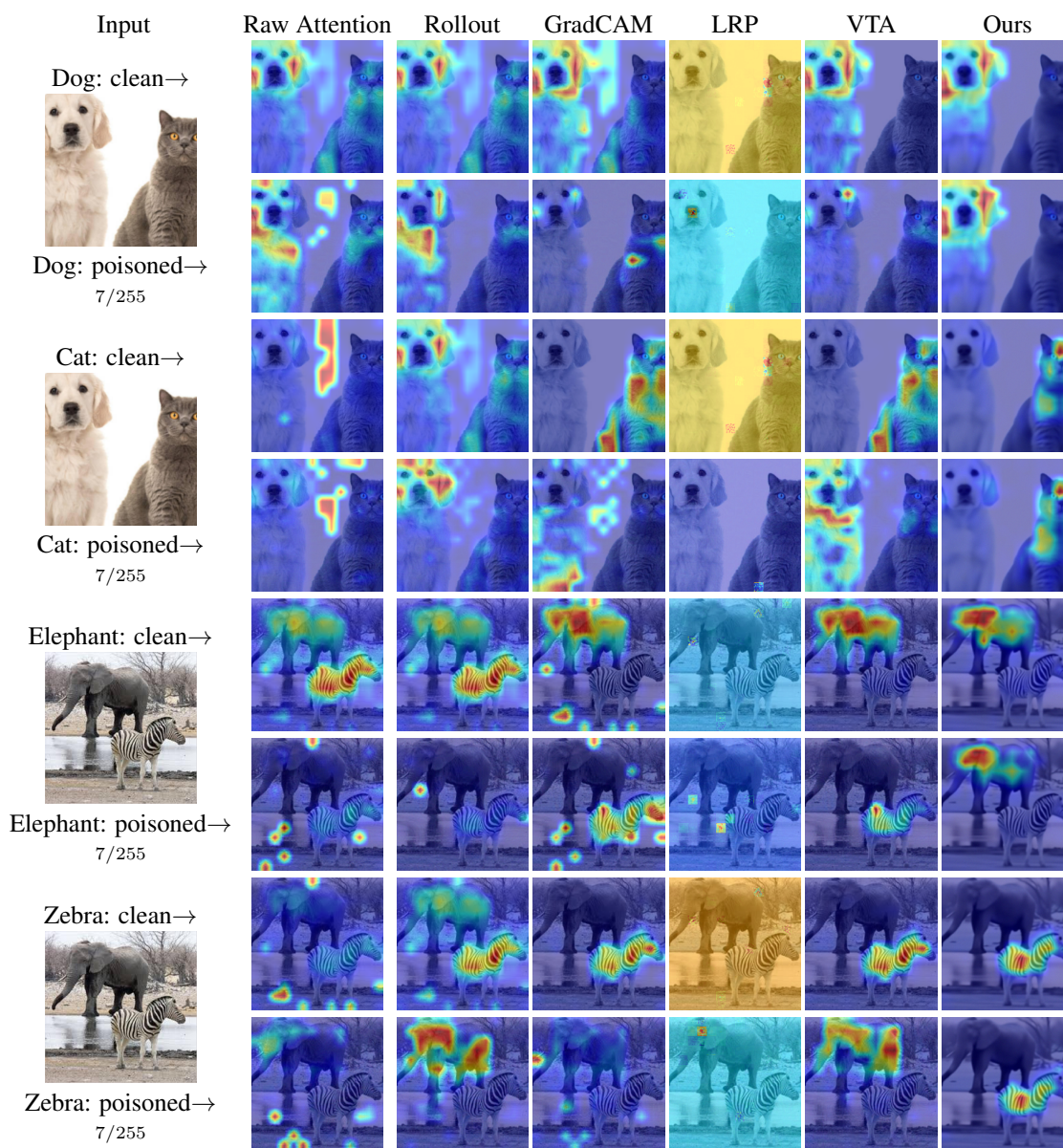


Figure 5: Class-specific visualizations under adversarial corruption.

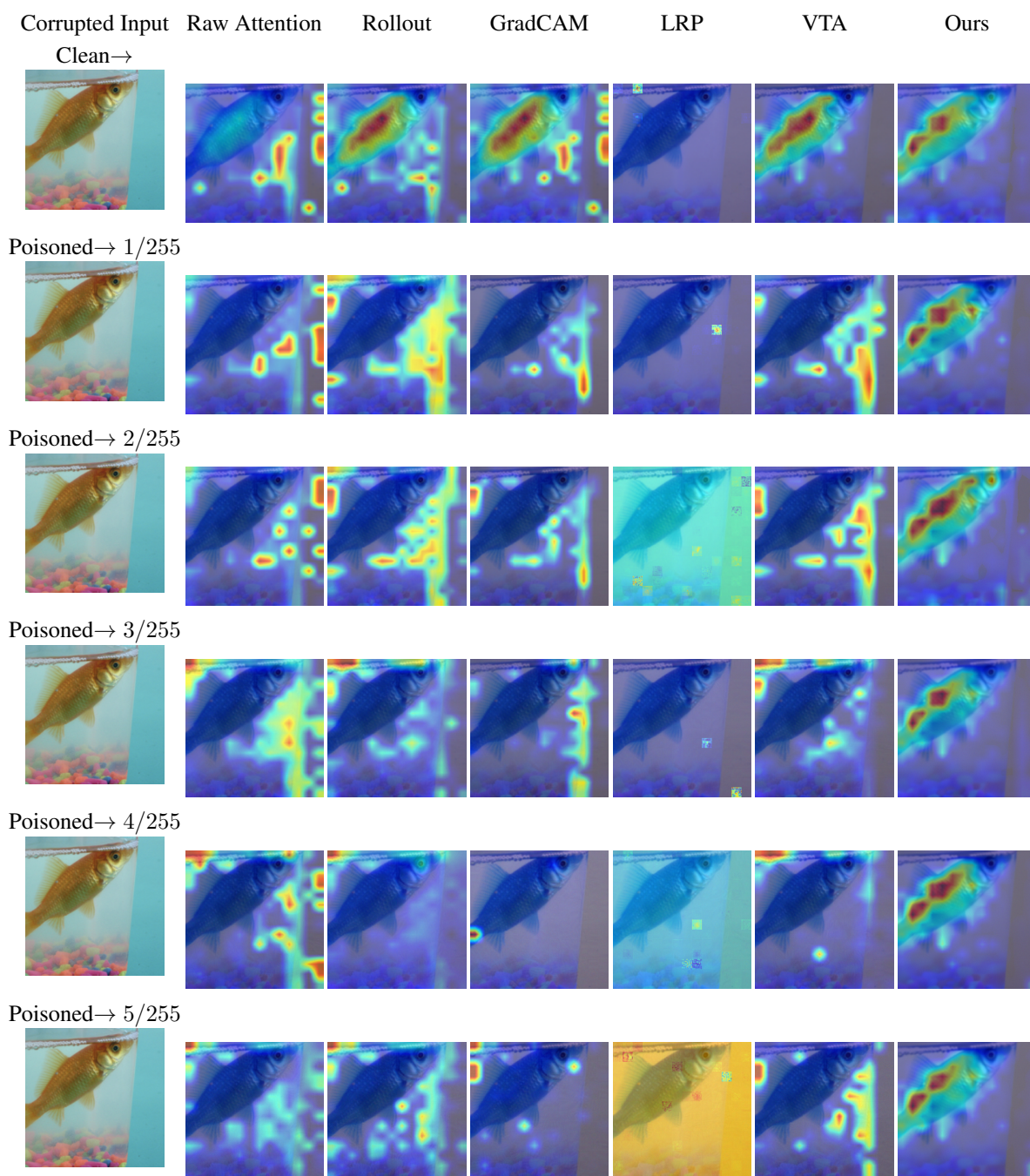


Figure 6: Visualization results of the attention map on corrupted input for different methods under different attack radii.

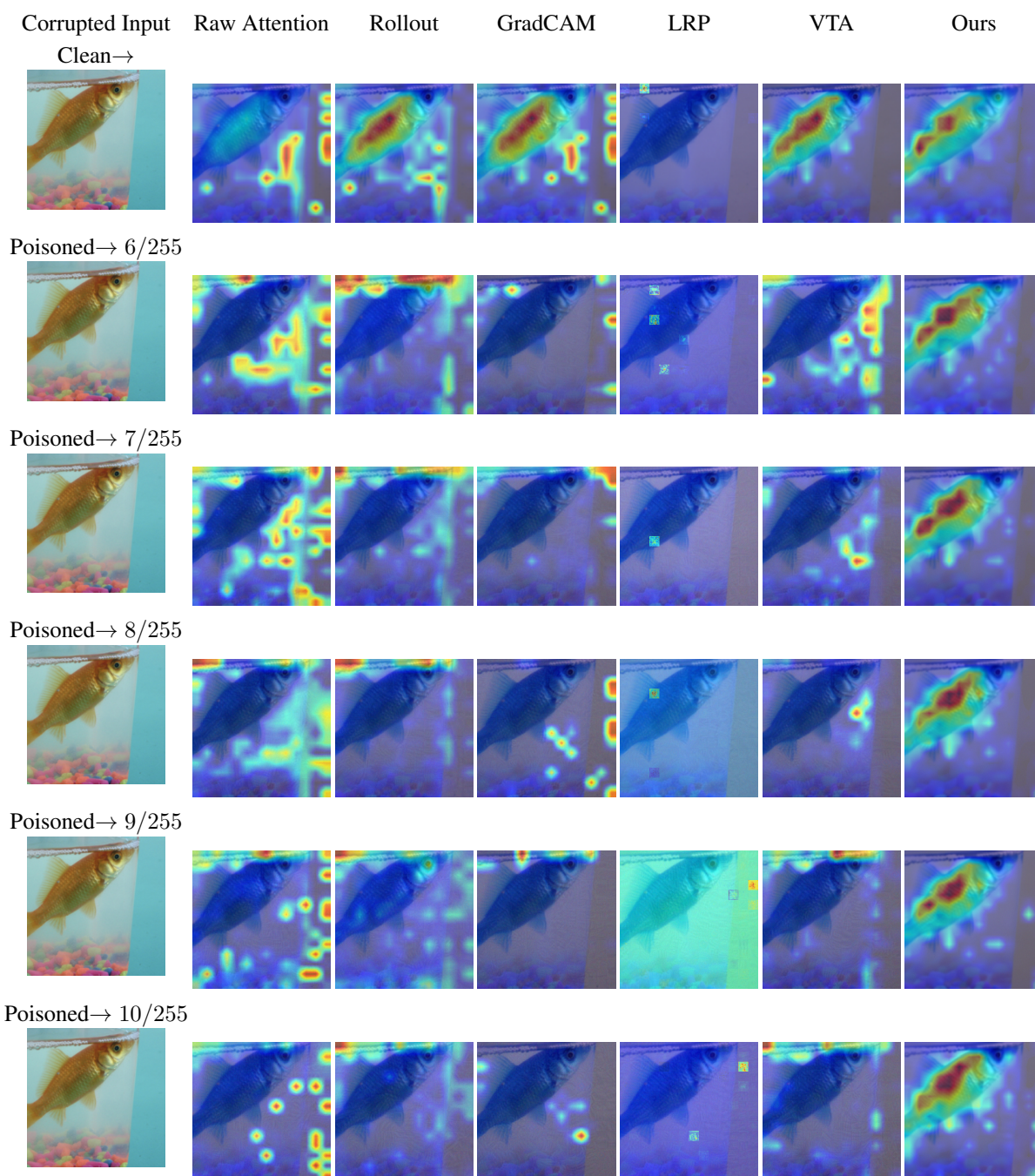


Figure 7: Visualization results of the attention map on corrupted input for different methods under different attack radii.

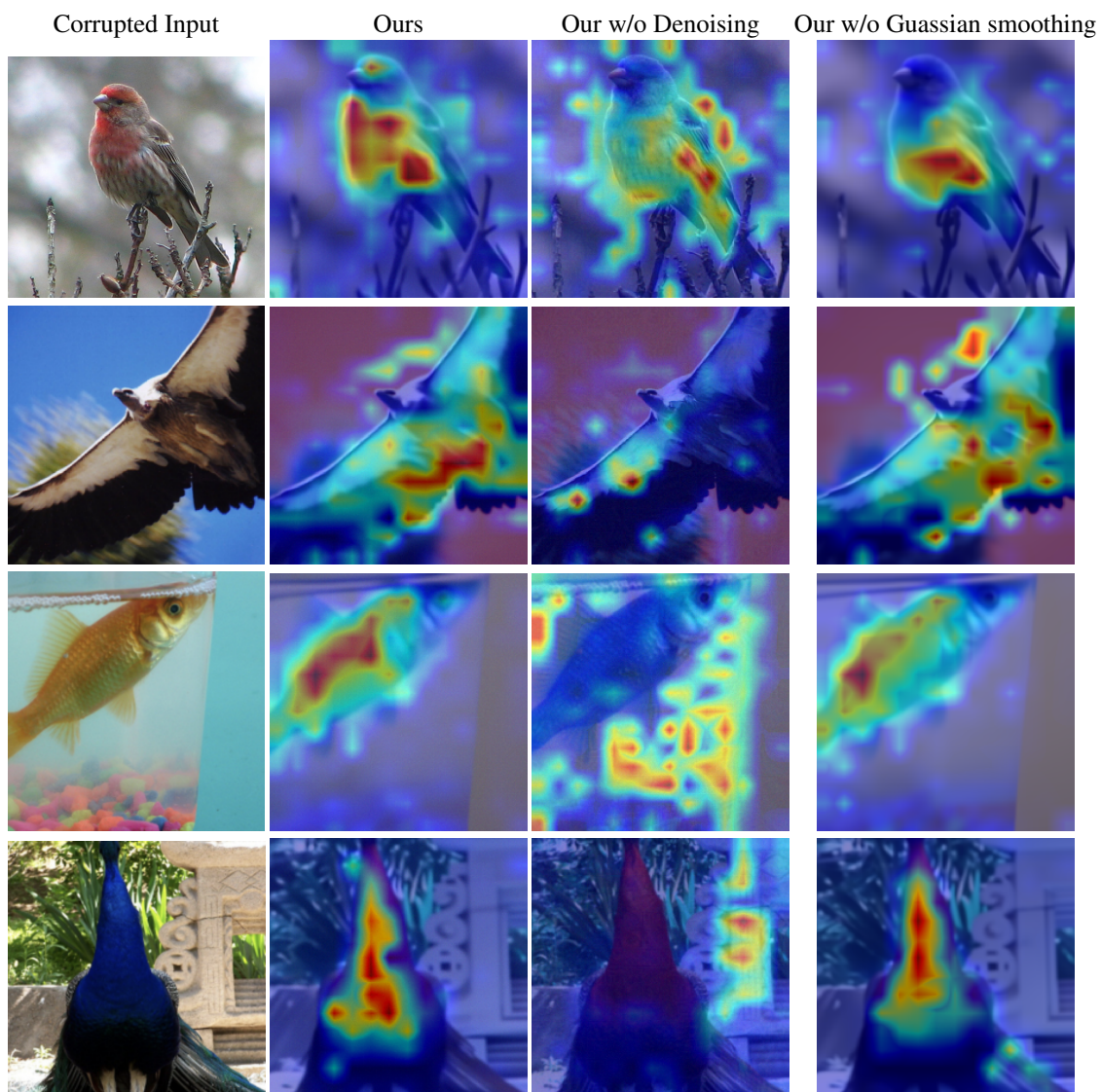


Figure 8: Visualization results of the attention map on corrupted input for the ablated version of our method.

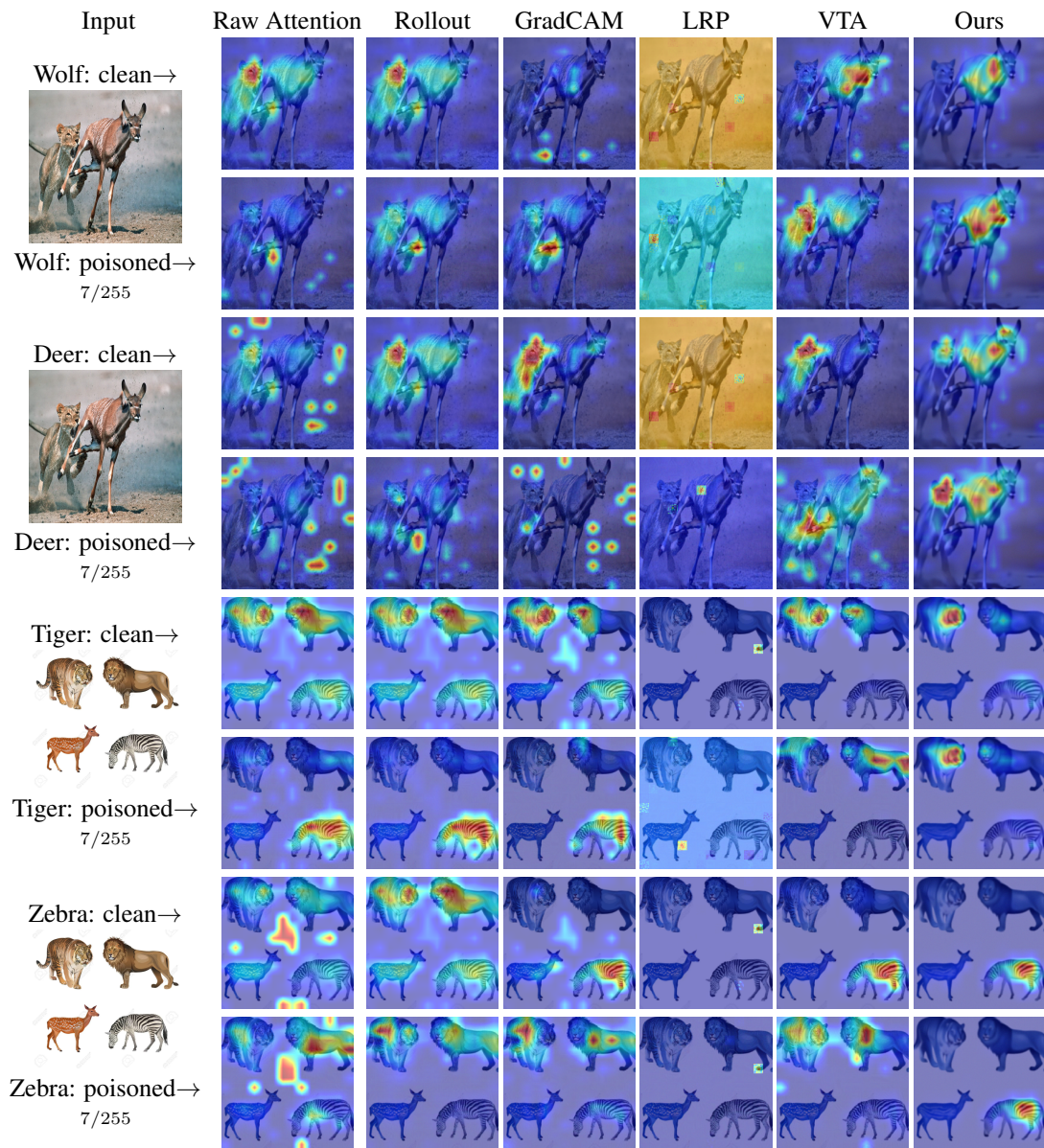


Figure 9: Class-specific visualizations under adversarial corruption. For each image, we present results for two different classes.